Peer reviewed version

Link to published version (if available):
10.1002/cnm.1393

Link to publication record in Explore Bristol Research
PDF-document

University of Bristol - Explore Bristol Research
General rights

Topological flow structures and stir mixing for steady flow in a peripheral bypass graft with uncertainty

A. M. Gambaruto*, A. Moura, A. Sequeira

CEMAT, Department of Mathematics, Instituto Superior Técnico, Technical University of Lisbon, Lisbon, Portugal

SUMMARY

With growing focus on patient specific studies, little attempt has yet been made to quantify the modelling uncertainty. Here uncertainty in both geometry definition obtained from in vivo MRI scans and mathematical models for blood are considered for a peripheral bypass graft. The approximate error bounds in computed measures are quantified from the flow field in steady state simulations with rigid walls assumption.

A brief outline of the medical image filtering and segmentation procedures is given, as well as virtual model reconstruction and surface smoothing. Diversities in these methods lead to variants of the virtual model definition, where the mean differences are within a pixel size. The blood is described here by either a Newtonian or a non-Newtonian Carreau constitutive model.

The impact of the uncertainty is considered with respect to clinically relevant data such as wall shear stress. This parameter is locally very sensitive to the surface definition, however variability in the topology has an effect on the core flow field and measures to study the flow structures are detailed and comparison performed. Integrated effect of the Lagrangian dynamics of the flow are presented in the form of stir mixing, which also has a strong clinical relevance.

1. INTRODUCTION

There is an increasing desire for highly resolved numerical simulations of *in vivo* data aimed at patient specific studies on a clinical basis, as well as targeted studies in idealised geometries that can yield insight into complex physiological processes. A key aspect in performing these works is the ability to understand and accurately reproduce the observations, in both the mathematical models that govern the processes as well as the setup of the problem. There is however an inherent uncertainty, or error, when obtaining data *in vivo*.

In this work we formulate a possible uncertainty range in the context of clinically relevant flow measures, highlighting general differences in the flow field and geometry definition. These are related to the methods used in the problem set up and rheological models in the numerical simulations. Specifically, we consider an example of a steady state flow for a patient specific distal peripheral end-to-side anastomosis configuration, where the health care concern is commonly re-stenosis and atherosclerosis. Measures to study the flow field focus on both wall and core flow, analysing the wall shear stress (WSS) as well as secondary flows and stir mixing.

---

*Correspondence to: agambar@math.ist.utl.pt; CEMAT, Department of Mathematics, Instituto Superior Técnico, Technical University of Lisbon, Lisbon, Portugal

Uncertainty in the problem set up stems from the virtual model preparation from the medical images [1]. In this work the same data set is used and two automatic methods for image segmentation are chosen from the existing image segmentation community [2] that are based on clustering. The initial surface definitions are obtained using a partition-of-unity implicit function approach to interpolate the stack of segmented cross-sections, yielding finally a piecewise linear triangulated mesh [3]. Different intensities of smoothing are applied to the surface definitions in order to remove noise and effects due to the pixelated nature of the medical images, as well as to observe the level and size of detail that influences the resulting flow field.

The models to describe the blood flow are undoubtedly of great importance in achieving accurate numerical simulations, such that the choice of appropriate model and its parameters introduces further variability and uncertainty. Throughout most of the arterial system of healthy individuals, the red blood cells are dispersed and it is considered sufficient to model blood as an inelastic, constant viscosity fluid (Newtonian) [4]. However, in some disease states, the vascular geometry is altered in such a manner as to sustain relatively stable regions of slow recirculation (e.g. aneurysms or downstream of a stenosis). In such flows, more complex constitutive models should be used [4, 5], like for instance shear-thinning and viscoelastic models [6]. In these cases, Newtonian models may underestimate the WSS in slow flow regions as opposed to non-Newtonian models, with a clear significance to healthcare. Furthermore, the selection of the non-Newtonian model or the value of the fixed viscosity in the case of a Newtonian model, will result in a change in the flow field that should be quantified with respect to uncertainty in the virtual model definition.

It is known that the haemodynamics in arteries is linked to disease formation such as atheroma and aneurysms, which are nowadays commonly studied. While the relationship between the flow field and disease are not fully understood, fluid mechanics parameters on and near the artery wall, such as WSS and derived measures, are among the most commonly sought correlators to disease [7, 8]. The non-planarity and tortuousity of vessels play a determining role in the arterial system [9], resulting in a strong influence of the local and upstream vessel topology on the flow field. In specific, for the case of distal end-to-side anastomoses, the core flow shows strong influence of non-planarity to secondary structures [10, 11, 12], principally vortical structures and separated flow regions. Secondary flow structure have also been studied in idealised circular non-planar geometries [13, 14] within a medical context. The association of the vessel topology on the flow still remains to be studied, especially with respect to small-scale geometric features (such as small surface irregulatiries), that can locally affect the derived flow parameters on or near the wall, as well as the local geometric features (such as stenoses and larger coherent surface features), that greater affects the core flow field.

In performing patient specific numerical studies based on *in vivo* measurements, there are a range of possible errors as detailed in [1]. Despite the importance in quantifying error bounds there has been relatively little work as regards to this, principally due to the difficulty in measuring the initial error bounds and how they propagate. Uncertainty in the geometry definition has been discussed in [1, 15, 16, 17, 18], all of which indicate a strong influence of the uncertainty or variation in the surface definition on the resulting flow field. The question of reproducibility in these woks is studied in terms of data comparison from multiple scans or varying medical image segmetnation schemes and intesities of surface smoothing.

The effect of different rheological models has been discussed in [18, 19, 20, 21, 22], showing marked differences between them. Comparison between rheological models and changes in geometry is presented in [18], where flow parameters on the wall are studied and the geometry uncertainty is given by multiple scans at weekly intervals of the same patient case, concluding that the geometry precision plays a dominating role as compared to non-Newtonian modelling. It should be noted however that the geometires studied in [18] are the carotid bifurcation where regions of recirculation were not present, and the range of shear rates is not large to bring about large changes in apparent viscosity, such that there are no dominating non-Newtonian effects. Furthermore [18] observes reproducibility by performing repetitions of scans at weekly

intervals while no sensitivity to the segmentation and virtual model reconstruction is directly discussed.

A means of validating the computed flow field is by the use of phase contrast MR by providing a detailed velocity map. Nevertheless, this imaging modality is still prone to inaccuracies, however it has been used to validate numerical simulations [23].

In this work a peripheral bypass graft is used to gauge the uncertainty given by both the virtual model definition as well as the choice of the viscosity function constitutive model for blood. The outline of the paper is as follows. Section 2 is dedicated to the virtual model preparation from medical images. In Section 3 the differences resulting in the virtual models are quantified based on the closest distance between the models, volume, surface area and the mean surface curvature. Section 4 discusses the fluid models used, the flow boundary conditions and details the mesh independence results. Section 5 introduces measures based on the velocity gradient tensor to identify topological features in the flow, while Section 6 presents an entropic measure of mixing with a novel improved resolution. Section 7 discusses the uncertainty by comparing the computed flow field with respect to the different geometries, investigating both flow measures on the no-slip boundary as well as in the free-slip domain. Finally, the conclusions are given in Section 8.

2. VIRTUAL MODEL PREPARATION

A large portion of patient specific studies that have investigated the effect of uncertainty in numerical simulations have concentrated on the use of different mathematical models and boundary conditions. However, there are few studies detailing effects of topological uncertainty stemming from *in vivo* data acquisition and its processing to obtain a 3D virtual model.

In this section the outline of procedures used in reconstructing the lumen boundary are detailed, namely: medical image segmentation, 3D surface interpolation, and virtual model surface smoothing.

The choice of this data set for a patient specific study is based on its use in previous works, investigating the effects of uncertainty on resulting WSS and correspondingly the clinical evaluation. The uncertainty was described by segmentation, surface smoothing and geometry idealisation based on fitting elliptical cross sections to the segmented contours [1]. Furthermore the data set is part of a study characterisation of peripheral bypass anastomosis geometry [24]. The histology of the patient involves re-occlusion by the 13th month post-operatively and the insertion of a jump graft which later also failed, as detailed in [25].

2.1. Patient Specific Data Set

The image data set is obtained using *Magnetic Resonance Imaging* (MRI) and comprises of 35 images in the axial plane with spatial resolution 256×256, interpolated to 512×512 pixels by K-space zero filling resulting in a pixel size of 0.254×0.254 mm size, and 1.5 mm slice thickness and spacing. The images were obtained from 2D TOF using a 1.5 Tesla machine. Spatial pre-saturation is used to suppress arterial flow, which can be noticed especially as a loss of signal in the proximal vessel.

The *Contrast-to-Noise Ratio* (CNR) is a measure to quantify the goodness of the image quality, defined here as $CNR = \frac{S_{ROI} - S_{ST}}{\sigma_{NOISE}}$, where S_{ROI} and S_{ST} are the mean signal intensities (or mean square amplitudes) of the region of interest (ROI) and the surrounding tissue (ST), respectively, and σ_{NOISE} is the standard deviation of the signal intensities of the surrounding ROI background. For the case studied $CNR \approx 2$ [1] on average for the image stack, which can be considered to be relatively good. Locally however, the value may differ and the regions of largest variations in the segmentation are identified to be at the regions of bypass and proximal stenoses, as well as parts of the anastomosis. These regions are locations of complex flow pattern or faster flow, which are known to affect the acquisition and hence yield greater uncertainty in the definition of the lumen boundary.
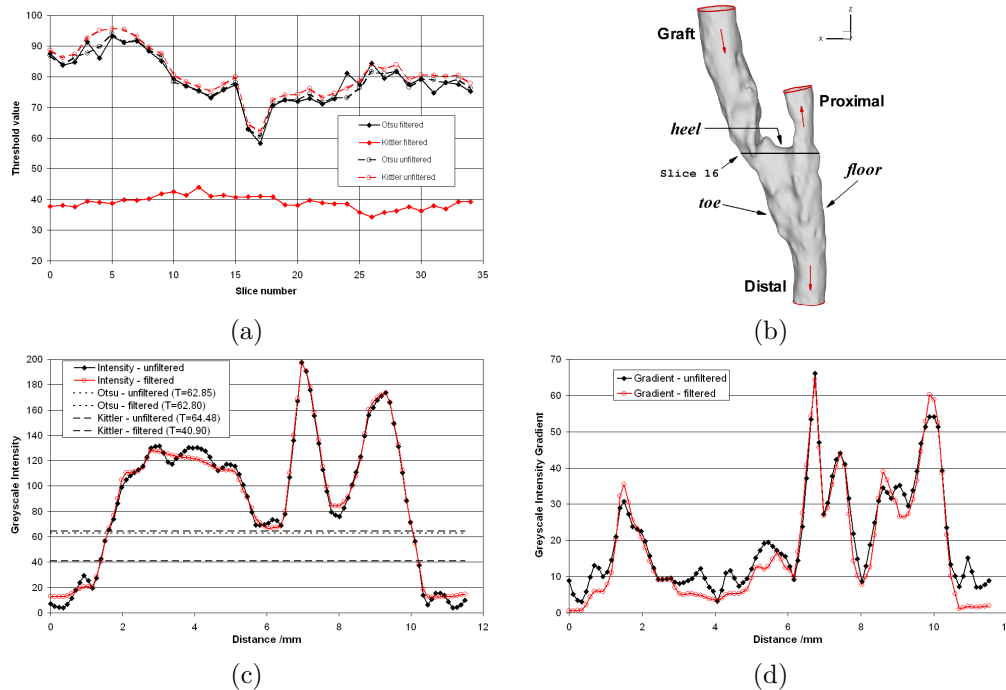
Figure 1. (a) Threshold variation along the image stack, where slice 0 corresponds to the distal extremity and between slice 16 and 17 lies the bifurcation to the bypass and proximal conduits. Location of slice 16 and nomenclature are shown in (b), as well as the flow direction. Variation of image intensity (c) and intensity gradient (d) are along the blue line shown in Figure 2 (going from bottom right to top left).

2.2. Medical Image Segmentation

Medical images obtained *in vivo* are susceptible to uncertainty in defining features that arise through both the imaging modality, as well as random noise. Unfortunately, there is no means of obtaining a 'ground truth' reconstructed virtual model from *in vivo* measurements, and uncertainty naturally arises. With the MRI modality used, the blood appears white while the background is black. A image with no uncertainty would be a binary image. Partial volume effects, patient movement, complex flow patterns and random noise are some of the main causes of unclear identification of features in medical images and a grey-scale is obtained instead of a binary image. The aim of accurate image segmentation is to identify two distinct classes: foreground and background, that are equivalent to a binary image.

The images are initially cropped to identify only the desired vessel using the *maximum intensity projection* (MIP). In doing this, the pertinent information is preserved and other regions containing undesired features and noise are removed. Thus, the desired feature is enhanced principally by removing undesired information in the image. Cropping the data set is also of importance to reduce the computational cost. Based on the cropped region, the pixel intensities are then normalised to range between 0-255, mainly to standardise in order to allow for comparison with different patient data sets.

Image filtering, as a means of de-noising, is then performed, using the popular Perona-Malik anisotropic diffusion method [26, 27]. The Perona-Malik filter is widely used despite being ill-conditioned [27]; in practice the only noticeable effect of this drawback is staircasing at slowly varying edges. Other filters as well as image contrast enhancement methods exist in the litterature, however the Perona-Malik filter is chosen due to its current widespread use, and the fact that it yields good results for our purposes, as shown in Figure 2.
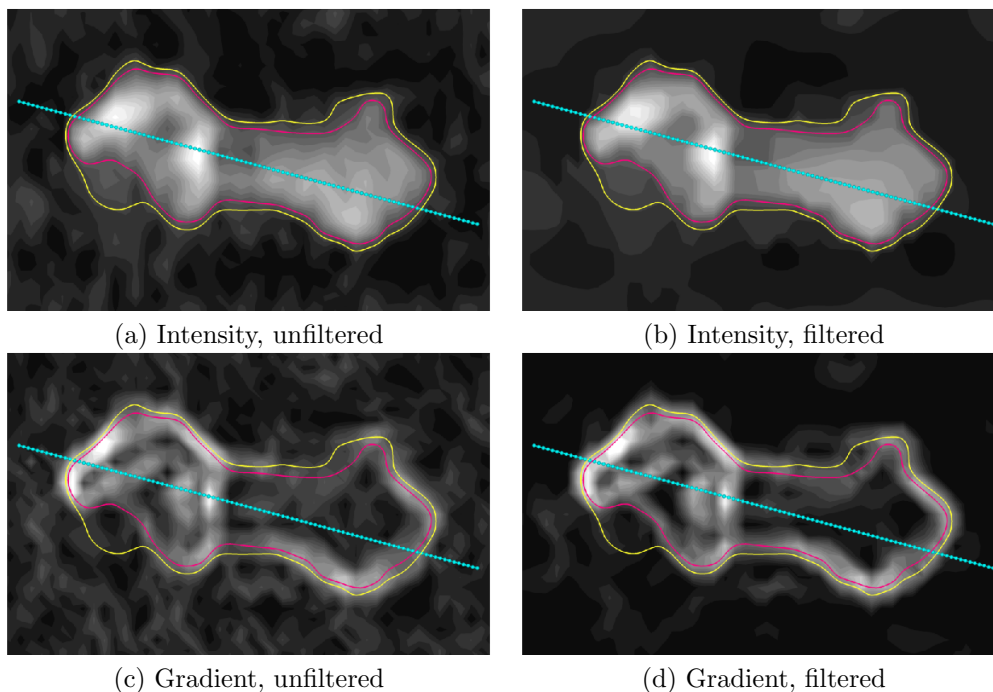
Figure 2. Contours of lumen boundary for Slice 16 (location shown in Figure 1b) superimposed over image intensity (a, b) and intensity gradient (c, d) for both the unfiltered (a, c) and filtered (b, d) image using the Perona-Malik filter. Segmentation is performed using the Otsu (red) and Kittler (yellow) methods.

Finally, a threshold value T of the pixel intensity is sought to delineate the foreground (desired object) from the background. In this way the background is given by $0 \leq t \leq T$ and the foreground by $T \leq t \leq 255$, where t is the individual pixel intensity. The thresholding techniques chosen are clustering methods, which use the grey level histogram of the image, and thus transforming the 2D image into a 1D signal, losing any spatial information of the image which may be a weakness in the methods. The two methods studied here are the Otsu [28] and the Kittler [29] methods, chosen due to their popularity and accuracy [2]. Segmentation is performed individually to slices, allowing the threshold value to vary within the stack but making it constant for each individual image. The segmentaion methods used in this study are now described briefly.

Otsu: The Otsu method [28] is among the most commonly used clustering methods due to its simplicity and robustness. The method is based on maximising the between-class variance, or equivalently minimising the within-class variance, and works well when the number of pixels in each class is similar. The algorithm consists in calculating the variance for a range of threshold values from lowest to highest, and then indicating the best threshold as that where the within-class variance is minimum.

Kittler: The Kittler method [29] is an iterative method that relies on fitting a Gaussian to the background and one to the foreground pixels in the histogram. The new threshold is obtained by solving a quadratic equation, and the value corresponds to the crossing location of the two Gaussians. The assumption is that the object and background pixel intensities are normally distributed. The Kittler method ranked top in the survey of [2].

Results of the grey-level thresholds for the image stack for the different methods is shown in Figure 1. Clustering methods are probabilistic and do not retain the image spatial information, however they are generally robust, automatic, and very inexpensive computationally. User

intervention in performing segmentation procedures may help in avoiding deficits in automatic methods, however it introduces variability and non-repeatability.

Other popular methods rely on the image intensity gradient or higher derivatives such as the Hessian and Laplacian, and their eigenvalues. Nevertheless, these can be more susceptible to noise due to the higher order derivatives, as well as partial volume effects and flow imaging artefacts in MRI. Means to overcome these drawbacks include smoothing as in deformable models, or the need for user assistance for intervention and correction. These methods have been seen to perform worse than clustering methods in certain cases [2]. Importantly, it is clear that there is no convergence to a common solution between methods, and the notion of uncertainty persists.

Observing the two virtual model definitions obtained before any adaptation is made, as shown in Figure 3, the Kittler method is capable of distinguishing the vessel from the background even where the contrast is poor, as noticeable by the greater length of proximal vessel being captured. However, the method appears to identify the conduits erroneously in other instances, as seen at the terminal portion of the distal conduit, where a bifurcation is clearly present and more accurately captured with the Otsu method.

In brief, we have chosen some popular, automatic and computationally inexpensive methods to obtain a range of possible segmentations and virtual models. These can be used to study the range of uncertainty in model boundary definition, and correspondingly the flow field and parameters postulated to be associated to disease. We note that while these methods proved well adapted to the patient case selected, other cases may be better adapted to different thresholding schemes.

2.3. Virtual Model Surface Reconstruction

Uncertainty in the segmentation is further augmented by the virtual model reconstruction that involves interpolation. Due to the medical image resolution, a direct extraction of the desired definition is not possible and an interpolation approach is required to allow for finer sampling. Large anisotropy of pixel to slice spacing may lead to greater uncertainty in the virtual model definition. The virtual model surfaces are obtained from the segmented contours using an implicit function formulation, also known as Kriging, with cubic radial basis function interpolation, as described in [1, 12].

The surface interpolating the segmented contour stack is defined as the zero-level iso-surface of an implicit function $f(\mathbf{x})$. Setting $f(\mathbf{x}) = 0$ on sampled points of the cross section stack defines the *on-surface* constraints. A gradient is formed in the implicit function by introducing further constraints at a constant close distance normal to the curve, known as *off-surface* constraints, with $f(\mathbf{x}) < -\alpha$ inside the curves and with $f(\mathbf{x}) > \alpha$ outside the curves, where α is a constant. The resulting problem is the solution of the unknown coefficients $\mathbf{c}$ from a linear system given by $f(\mathbf{x}_i) = \sum_{j=1}^{n} \mathbf{c}_j \phi(\mathbf{x}_i - \mathbf{x}_j)$, for $i = 1, \ldots, n$, where ϕ is the radial basis function. To minimise curvature variation, the cubic radial basis function is used $\phi(\mathbf{x}_i - \mathbf{x}_j) = |\mathbf{x}_i - \mathbf{x}_j|^3$, where $\mathbf{x}_i$ are the position vectors the function is evaluated at, and $\mathbf{x}_j$ are the position vectors of the interpolation constraints.

The zero-level iso-surface of the implicit function, that defines the virtual model surfaces, is extracted using the marching tetrahedra approach [30] with linear interpolation to give an initial triangulation, that is then projected onto the true iso-surface to eliminate the discretisation errors in the linear interpolation.

To reduce the computational time in the implicit function formulation as well as the marching tetrahedra method, a partition-of-unity approach [31, 32] is applied. Thus, the global domain of interest is divided into smaller overlapping subdomains where the problem can be solved locally. The local solutions are combined together by using weighting functions that act as smooth blending functions to obtain the global solution. The domain is divided into rectangular subdomain partitions, using C^1 base spline functions $V(d_i) = 2d_i^3 - 3d_i^2 + 1$ as the weighting functions over each subdomain, where $d_i = 1 - \prod_{r \in x,y,z} \frac{4(p_r - S_r)(T_r - p_r)}{(T_r - S_r)^2}$, and S_r and T_r are

opposite rectangle subdomain corners, such that $0 \leq d_i \leq 1$ with $d_i = 1$ on the edges and $d_i = 0$ in the centre. Hence $V(0) = 1, V(1) = 0, V'(0) = 0, V'(1) = 0$.

2.4. Surface Smoothing

Due to the pixelated nature and the presence of uncertainty and noise in the medical images, the resulting virtual model surfaces are unrealistically rough and surface smoothing is necessary. Care is taken in the smoothing procedure to ensure fidelity with the medical images. The method adopted is a variation to that described in [1].

The algorithm has two stages. The first stage of the smoothing is an explicit scheme where the severity of smoothing increases with the number of iterations performed. This employs the bi-Laplacian method [33] which involves moving the mesh nodes using the local mesh connectivity information in order to minimise the surface roughness, and hence curvature variation. In the second stage of the smoothing method, the surface area and volume alterations brought about are reduced by an iterative uniform inflation of the surface along the local normal [1, 3].

The first stage is detailed as follows. Consider a regular triangular mesh consisting of n vertices $\mathbf{v}_i = (x_i, y_i, z_i)$, $i = 1, \ldots, n$. The vertices neighbouring each vertex $\mathbf{v}_i$ in the triangulation are denoted by $\mathbf{v}_j$, $j = 1, \ldots, m_i$, where m_i is the number of neighbours. The discrete Laplacian at the vertex $\mathbf{v}_i$ is calculated as

$$\mathbf{L}_i = \sum_{j=1}^{m_i} w_{ij}(\mathbf{v}_j - \mathbf{v}_i),\tag{1}$$

where the weights w_{ij} have the constraint that $\sum_{j=1}^{m_i} w_{ij} = 1$. Here $w_{ij} = 1/m_i$ is used, and hence the Laplacian can be interpreted as the vector moving the node in question to the barycentre of the neighbour vertices, which is stable and regularises the mesh.

The iterative smoothing is performed in two sub-steps as

$$\begin{cases} \mathbf{v}_i^{k+1/2} &= \mathbf{v}_i^k + \lambda \mathbf{L}_i^k, \\ \mathbf{v}_i^{k+1} &= \mathbf{v}_i^{k+1/2} + \mu \mathbf{L}_i^{k+1/2}, \end{cases}$$

where k denotes the iteration number and the Laplacian is recalculated at each sub-step. The mesh nodes are moved simultaneously at the end of each sub-step. Here we take $\mu = -\lambda$, corresponding to the bi-Laplacian smoothing, which is analogous to the minimisation of the thin plate energy of the surface [33]. The method can be thought as two Laplacian smoothing steps, the first step as an explicit iterative solution to the diffusion equation where the curvature is the property diffused, while the second step is used to inflate the surface and yield a bi-Laplacian overall method. For this work all the bi-Laplacian smoothing iterations are performed using $\lambda = 0.6$.

If the curvature on a surface can be thought of as a signal, then the reduction of the high curvature is analogous to convolution of the curvature signal with a low-pass filter [34]. Therefore, the bi-Laplacian method acts as an overall low-pass filter with no compensation (or gain), with the result that the geometry tends to shrink. A variation of the bi-Laplacian method is given by [35] with $\mu < -\lambda$ to compensate for shrinkage during smoothing, that is equivalent to amplifying the low-frequency signal (hence the low curvature) while filtering the higher frequencies; however this leads to topological distortions and does not gurantee minimum shrinkage. The criterion adopted to minimise both the surface area and volume changes in the iterative smoothing stage is to introduce a second stage that involves an iterative uniform inflation of the surface along the local normal until the distance between the smoothed and the original surface representations is minimised [1].

The reconstructed geometries obtained using the Otsu and Kittler segmentations are smoothed using 50 bi-Laplacian iterations in order to reduce faceted features for quality mesh preparation. This can be considered as not altering the surface definition since the deformation to the surface was found to be a maximum of 0.1 pixels, on average less than 3% pixel and over
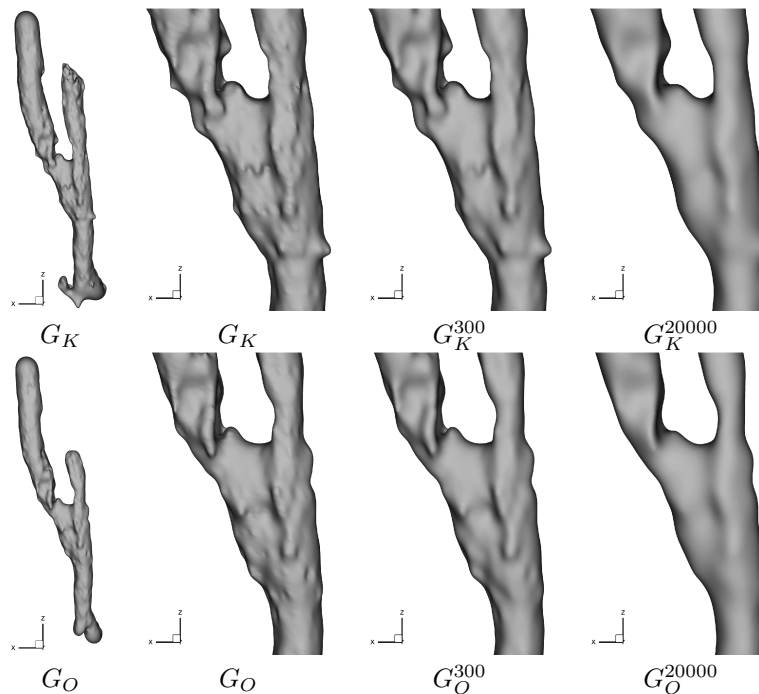
Figure 3. Reconstructed virtual models and detail of anastomosis obtained from the Kittler and Otsu segmentation methods, with detail shown for different levels of smoothing: un-smoothed (G_K, G_O), slightly smoothed (G_K^{300}, G_O^{300}) and intensely smoothed (G_K^{20000}, G_O^{20000}).

90% of the surface changes by less than 4% pixel. Further iterations in the surface smoothing lead to simplified geometries, where the small-scale features present in regions of high curvature are progressively removed.

In order to understand the significance of small-scale geometrical features on the flow, in this work the geometries are further subjected to 300 and 20000 iterations (on top of the 50 iterations mentioned above) of the bi-Laplacian smoothing. The small-scale uncertainties may be due to noise or imaging artefacts such as the partial volume effects and flow related artefacts. Nevertheless, it is plausible that these small scale features are anatomically correct and the surface smoothing can then be considered as an idealisation process by removing detail. It is important to note that large-scale geometric features are preserved, such as conduit bifurcation angles (analysed using the discrete method discussed in [1] and references therein), while surface area and volume changes are minimised as mentioned above.

Once the mathematical models to describe the fluid have been chosen, the flow field is described by the flow boundary conditions and the geometry definition. By reducing the level of detail by smoothing the surface, the fluid properties at or near the wall, such as WSS and spatial gradients of WSS, will inevitably change [1]. Yet, it is not clear to what extent and how far reaching into the flow core the impact of these small-scale changes in the geometry definition will be.

In this manner, uncertainty in boundary definition is studied with respect to two automatic segmentation methods and the level of small scale detail. To summarise, the geometries studied are obtained by the Otsu and Kittler thresholding methods and subjected to moderate and intensive smoothing. The resulting geometries are denoted by G_O, G_O^{300}, G_O^{20000}, G_K, G_K^{300}, G_K^{20000}, where the subscript denotes the segmentation method and the superscript denotes the level of smoothing. The results presented are for the Newtonian fluid model case unless otherwise stated or marked as an additional subscript '$Carreau$', for example $G_{O-Carreau}^{300}$.

(a) Otsu segmentation, intensity

(b) Otsu segmentation, gradient

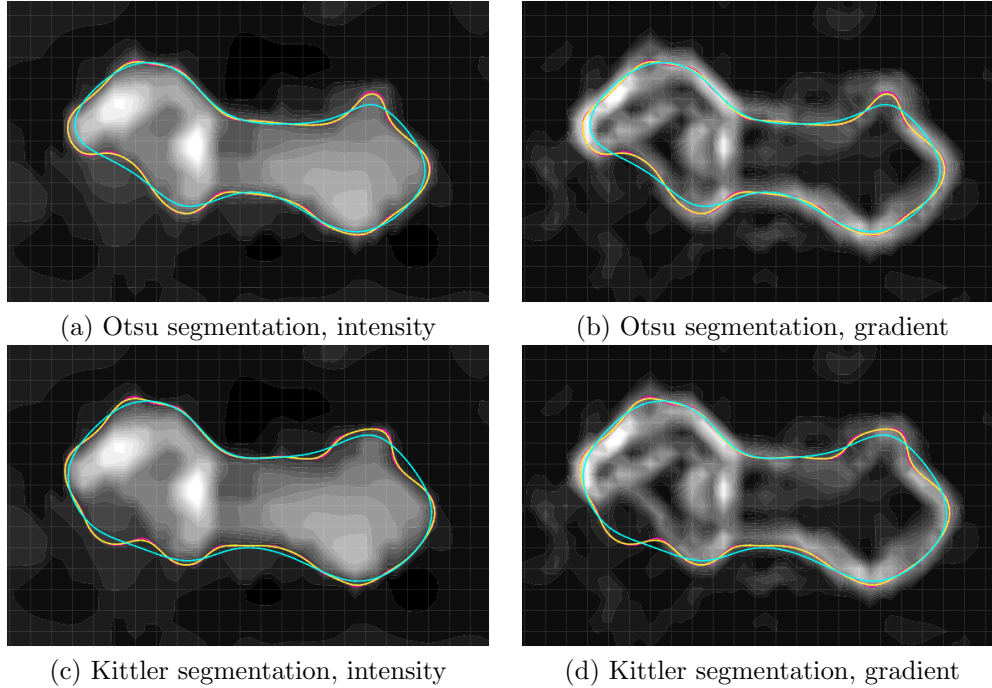(c) Kittler segmentation, intensity

(d) Kittler segmentation, gradient

Figure 4. Contours of lumen boundary for Slice 16 for the smoothed geometry definitions: red for G_O and G_K, yellow for G_O^{300} and G_K^{300}, and light blue for G_O^{20000} and G_K^{20000}. Top row shows cross sections obtained from the Otsu segmentation and bottom row for the Kittler segmentation. Contours are superimposed over image intensity (a, c) and intensity gradient (b, d) for the filtered image using the Perona-Malik filter.

3. TOPOLOGICAL DIFFERENCES IN SURFACE MODEL DEFINITIONS

In order to observe topological changes in the model definitions that are local or small-scale, the description of surface non-uniformity may be given by the curvature. The closed geometry which possesses the least amount of detail is a sphere, since it has a constant radius of curvature. Any change in the surface definition would induce a change in the tangent variation and hence a non-uniform curvature. In the smoothing described above, the curvature variation is reduced, and in so doing the level of small-scale features are attenuated.

The mean curvature at each node is calculated using the method proposed in [34] directly on a piecewise linear triangular mesh. It is given by

$$\kappa_i = \frac{1}{4A_i} \sum_{j=1}^{m_i} ||(\cot(\alpha_j) + \cot(\beta_j))(\mathbf{v}_j - \mathbf{v}_i)||, \qquad i = 1, \ldots, n, \tag{2}$$

where A_i is the area of the triangles surrounding the node $\mathbf{v}_i$, and α_j and β_j are the angles opposite to side ij in the triangles sharing this side.

The original and smoothed geometries can be seen in Figure 5 coloured by the curvature. The average surface curvature for G_K and G_O over the anastomosis region are approximately equivalent, however there is a reduction of approximately 15% and 35% between these and their smoothed variants using 300 and 20000 smoothing iterations, respectively.

Another means to quantify the difference between the models is the closest distance between surface definitions, that is a measure of the local change. Details are presented in Table I. It is clear that the absolute closest distance between the geometries lies within the pixel (0.254 mm) value on average, and hence within the uncertainty bounds of medical image resolution. On

Model comparison	Average	Standard Deviation	Peak
$G_K \rightarrow G_O$	0.25	0.14	1.0
$G_K \rightarrow G_K^{300}$	8×10^{-3}	9×10^{-3}	0.12
$G_K \rightarrow G_K^{20000}$	48×10^{-3}	50×10^{-3}	0.47
$G_O \rightarrow G_O^{300}$	7×10^{-3}	8×10^{-3}	0.10
$G_O \rightarrow G_O^{20000}$	45×10^{-3}	49×10^{-3}	0.41

Table I. Absolute closest distance between surface definitions as mean values, standard deviation and maximum values (mm). Note that 0.254 mm = 1 pixel.
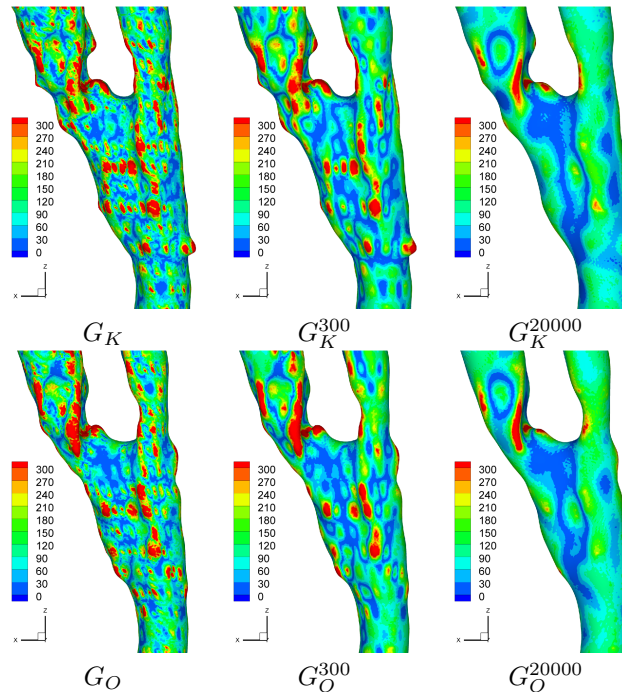

Figure 5. Surface mean curvature, as given by equation (2), for the geometries studied.

the other hand, locally the displacement can be of the order of a few pixels, nonetheless, from the standard deviation, this is seen to involve small regions.

A cross section through the smoothed geometries is presented in Figure 4. It is apparent that there is a great discrepancy between G_K and G_O due to the different consideration of uncertainty inherent of medical images. The G_K^{20000} and G_O^{20000} intensely smoothed geometries clearly do not follow the original segmentations of the lumen and there is arguably a lack of fidelity to the raw data. The G_K^{300} and G_O^{300} geometries however clearly respect the original segmentations and behave as smoother interpolations to the medical image data. Having said this, it is still unknown which best fits the true anatomic surface definition from the reconstructed virtual models.

Measures used in classifying large scale topological features of peripheral bypass grafts are predominantly the bifurcation angles of the conduits [24], giving an indication of planarity. In this work these angles do not perceivably change, as calculated by the discrete methods discussed in [1, 24], and other large-scale comparative measures are sought. These can simply be the surface area and volume of the geometry. It is found that the Kittler segmentations have an increased surface area of ∼15% and volume of ∼30% with respect to the Otsu segmentations, for the anastomosis region only. Calculating the ratio of volume to surface area, as a similar concept to the hydraulic diameter, it is found to be ∼0.9 for the Otsu and ∼1.0 for the Kittler
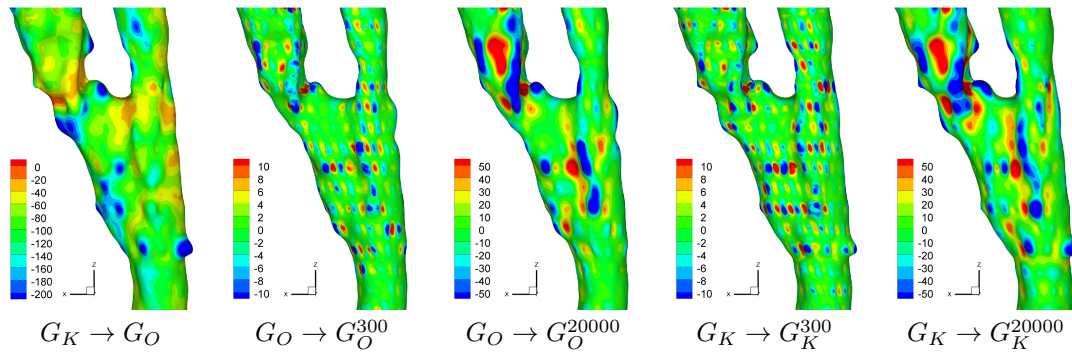
Figure 6. Distance map between geometries, measured as the closest distance from surface shown to target surface. The scale is in % pixels, where negative is inside the domain and positive outside.

segmentaions. From these measures one can estimate a greater traction force per unit volume in the Otsu cases, hence a greater pressure loss. The geometric variation is thus confined to the small-scale features, whilst the global features of the geometry are largely invariant with respect to bifurcation angles, but discernible as regards to volume and surface areas.

It can be seen from the threshold plots in Figure 1 that the methods perform substantially differently when the images are filtered, with the Kittler method having a lower threshold than the Otsu method, resulting in a geometry definition with increased patency. The locations of the biggest difference are seen from Figure 6, for both segmentation and smoothing variants of the geometries. The difference in the segmentation methods is apparently less obvious for the graft, upstream to the stenosis. Overall the closest distance map appears uniform, with a typical variation in surface definition under the pixel size, and the greatest differences localised in regions at the graft and proximal vessel junction to the anastomosis (which are stenosis locations), as well as the anastomosis 'toe' (which is a region of recirculating flow). It is clear that the smoothing performed with 300 bi-Laplacian iterations has had the effect of reducing noise carried through from both the pixelated nature of the medical images, and the location of the constraints in the implicit function formulation. In this case, the isolated regions of higher curvature have been removed and the deformation to the surface is largely in small isolated spots of varying sign.

4. MATHEMATICAL MODELS FOR CFD

The mathematical model describing blood flow in 3D regions of the cardiovascular system consists of the equations for the isothermal flow of incompressible fluids. In this study we consider the rigid wall and steady state flow assumptions as acceptable conditions to obtain preliminary results. While unsteady simulations and moving boundaries are more physiologically realistic, further variability is introduced when considering the waveform and the constitutive models for the vessel walls. Studies on the simplifications adopted indicate that the flow structures which dominate under unsteady conditions are qualitatively similar to those present in the corresponding steady flow computation [23, 10, 24]. Moreover it has been shown that the temporal average of WSS for unsteady simulations is close to the value of the WSS found for the steady case [19]. It is worth also noting that periferal arteries show a less pronounced pulsatility of the blood flow, though the waveform may be more complex than in other parts of the arterial system.

The equations in the computational domain Ω, are in this case given by:

$$
\begin{cases}
\rho\, \mathbf{u} \cdot \nabla \mathbf{u} - \operatorname{div} \boldsymbol{\sigma}(\mathbf{u}, P) &= \mathbf{0}, \qquad \text{in } \Omega, \\
\operatorname{div} \mathbf{u} &= 0, \qquad \text{in } \Omega,
\end{cases}
\tag{3}
$$

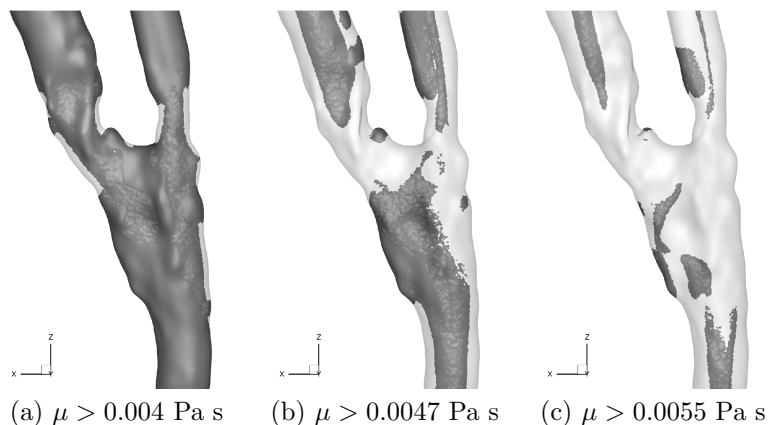(a) $\mu > 0.004$ Pa s   (b) $\mu > 0.0047$ Pa s   (c) $\mu > 0.0055$ Pa s

Figure 7. For $G^{300}_{O-Carreau}$, regions indicated are where the apparent viscosity calculated from the Carreau model used is greater than (a) 0.004, (b) 0.0047, and (c) 0.0055 Pa s. Note that regions identified in (b) correspond to low shear rates with $\dot{\gamma} < 100 s^{-1}$.

where ρ is the density of blood. The unknowns are the velocity $\mathbf{u}$ and the pressure P, while $\boldsymbol{\sigma}(\mathbf{u}, P)$ is the Cauchy stress tensor, described through a constitutive relation characterising the rheology of the fluid. Indeed, system (3) needs to be closed through a constitutive law, relating the Cauchy stress tensor with the kinematic quantities, velocity and pressure. Very often in literature blood is considered to be Newtonian, for which the consitutive relation is simply

$$\boldsymbol{\sigma}(\mathbf{u}, P) = -P\mathbf{I} + 2\mu\mathbf{D}(\mathbf{u}),$$

where μ is the constant blood viscosity and $\mathbf{D}$ is the strain rate tensor, given by

$$\mathbf{D}(\mathbf{u}) = \frac{1}{2}\left(\nabla\mathbf{u} + \nabla\mathbf{u}^T\right).$$

However, whole blood is a concentrated suspension of formed cellular elements, including red blood cells (RBCs), white blood cells, and platelets, suspended in an aqueous polymer solution, the plasma, which confer to blood a complex rheological behaviour (see for instance [4, 5] for reviews on rheological models for blood). It is known that blood exhibits marked non-Newtonian characteristics, particularly at low shear rates, which are mainly due to the behaviour of RBCs, that appear in high concentration compared to the other formed elements. One of the non-Newtonian properties displayed by blood is a shear-thinning viscosity, which means that blood viscosity decreases with increasing shear rate, defined as

$$\dot{\gamma} = \sqrt{\frac{1}{2}\left(\nabla\mathbf{u} + \nabla\mathbf{u}^T\right) : \left(\nabla\mathbf{u} + \nabla\mathbf{u}^T\right)}.$$

This mechanical property is attributed to the aggregation of RBCs in microstructures called *rouleaux*, which can themselves aggregate in secondary 3D micro-structures, at very low shear rates. On the other hand, for high shear rates these aggregates tend to rupture and RBCs elongate and align with the flow, decreasing the apparent viscosity of blood. It has been argued elsewhere that, due to the pulsatile nature of blood flow in large vessels and the time interval of the cardiac cycle aggregates do not have time to form and blood viscosity is overall constant and equal to its apparent viscosity at high shear rates ($\dot{\gamma} > 100 s^{-1}$), that is found to be around $\mu = 0.0035$ Pa s [36]. However, this is a simplifying assumption that should be taken carefully. The non-Newtonian behaviour of blood is important when the flow is decelerating and close to zero, experiencing low shear, that is, less than $100\ s^{-1}$, for the length of time for the 3D aggregates to form. This is significant for 30% of the cardiac cycle [20, 19]. For
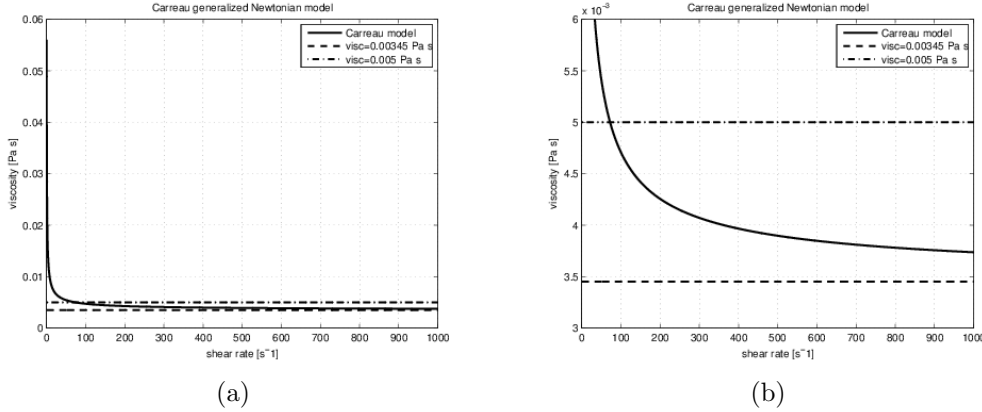
(a)   (b)

Figure 8. Varying viscosity $(Pa\ s)$ with the shear rate (s^{-1}) in the Carreau shear-thinning model, showing asymptotic behaviour (a) and detail (b).

instance, the shear rate may range from 0 s^{-1} to 1000 s^{-1} [20, 36] over the cardiac cycle, and regions of the core flow field where the shear rate is under 100 s^{-1} appear, leading to regions of higher viscosity. This can be particularly important in pathological situations of clinical inteterest, such as aneurysms or stenosis, or in the case of diseases like anemia [4]. Regions of apparent viscosity, related to the shear rates, are shown in Figure 7, indicating that for the case studied large portions of the domain are influenced by the non-Newtonian shear-thinning modelling. The region of separated flow at the anastomosis 'toe' and the centreline of the core flow exhibit markedly higher viscosities.

Other non-Newtonian properties of blood, such as viscoelasticity and yield-stress, have also been reported and studied [6, 4]. However these properties are less pronounced than the shear-thinning behaviour and will not be included in the modelling here. Another phenomenon of blood is its thixotropic behaviour, hence the time dependent change of viscosity related to the aggregation or disaggregation of RBCs. The equilibria of the RBC aggregate structures are found to be reached faster for higher shear rates, and more gradually for the lower ones [4, 5], with the time scale being greater than the cardiac cycle. However structures, and hence the shear-thinning non-Newtonian property, may be present despite not being in equilibrium. It should be noted that the non-Newtonian model used here is not time dependent but related only to the shear rate.

Here we consider two different constitutive models for the blood flow and compare them. In order to account for the shear-thinning behaviour of blood we use the Carreau *generalised Newtonian* constitutive model, given by:

$$\boldsymbol{\sigma}(\mathbf{u}, P) = -P\mathbf{I} + 2\mu(\dot{\gamma})\mathbf{D}(\mathbf{u}), \quad \text{with} \quad \mu(\dot{\gamma}) = \mu_\infty + (\mu_0 - \mu_\infty) \cdot \left(1 + (\lambda\dot{\gamma})^2\right)^{\frac{n-1}{2}}.$$

where $\lambda > 0$, and $n \in \mathbb{R}$ are constants to be estimated by curve fitting of experimental data (see [4]). In particular we take $\mu_0 = 0.056$ Pa s, $\mu_\infty = 0.00345$ Pa s, $\lambda = 3.313$ s and $n = 0.3568$ [37]. In Figure 8 the apparent viscosity as a function of the shear rate for the Carreau model with these parameters is represented.

The coefficients μ_0 and μ_∞ are the asymptotic viscosities, with μ_∞ the viscosity at the highest shear rate, and μ_0 the viscosity for the lowest shear rate. Notice that this model describes a shear-thinning behaviour for $n < 1$.

We also consider a Newtonian fluid with a constant viscosity near to μ_∞, corresponding to high shear rates, in particular, with $\mu = 0.004$ Pa s. This appears to be a good choice for the Newtonian constant viscosity, as it will be discussed later in Section 7, and it has also been commonly used in literature [24]. Other values of $\mu = 0.0035$ Pa s and $\mu = 0.0046$ Pa s are used, the latter being the average viscosity for $G_{O-Carreau}$.

The fluid equations (3) should be endowed with boundary conditions. On the physical wall boundary the no-slip condition $\mathbf{u} = \mathbf{0}$ is used, since a rigid wall model is considered. On the artificial boundary sections, created due to the domain truncation, a parabolic velocity profile is imposed with a mean velocity of $0.1 \, \mathrm{m \, s^{-1}}$ on the inflow section, corresponding to a Poiseuille flow. Specifically, the profile is given by $u = 2\bar{u}(1 - (r/R)^2)$, where R is the vessel radius, r is the distance from the cross section centre, and $\bar{u}$ is the mean cross section velocity. The mean velocity $\bar{u}$ was obtained *in vivo* using ultrasound. In order to perform this the inflow boundary is extended to a circular section. On the outflow sections the boundary is also extended to a circular section, so as to reduce the sensitivity of boundary conditions in the anastomosis region, and a flow division of 40% proximal and 60% distal is imposed. Both inflow and outflow boundary conditions are obtained from *in vivo* measurements.

By imposing the same mean velocity for all the cases studied, and since the Kittler and Otsu derived geometries are of different calibre, the Reynods number at the bypass graft inflow is found to be $Re = 125$ and $Re = 113$, respectively. Since Re is the ratio of inertial to viscous forces, we expect a difference in the flow field due to this, especially in the identification of core flow structures and WSS. If considering flow in a straight pipe with calibres the same as the bypass inflow section, the WSS is found to be 0.66 and 0.73 Pa, for the Kittler and Otsu segmentations respectively. The scaling is therefore approximately of 10% and should be kept in mind when analysing the results, nevertheless it is part of the uncertainty associated to performing patient specific studies from data obtained *in vivo*. It should also be noted that by imposing a constant mean velocity inflow the mass flow rate is also not preserved for the different geometries. Nonetheless for a constant velocity boundary condition, the WSS scales linearly to the diameter, however a cubic scaling is given if a constant flow rate is imposed [38]. Hence by fixing the mean inlet velocity the WSS difference has been minimised between the geometries studied.

The equations are solved by means of the finite volume method (using Fluent, Fluent Inc., Lebanon, USA), and allows to define both a constant viscosity or to use a Carreau generalised Newtonian model, by introducing its parameters. The volume mesh consisted in an unstructured mesh with approximate 0.13 mm edge length, resulting in approximately 3×10^6 elements. To ensure mesh independence, a 7.5×10^6 element mesh was used to compare the WSS values, obtaining differences less than 1% on average between meshes of different resolutions. More noticeable discrepancies in isolated spots were present. These were due to small changes (~ 0.1 mm) in the regions defining the separated flow, as well as to the jet orientation (from the graft into the anastomosis) that is descernible by a shift in the impingement location (which moved by 0.08 mm approximately).

5. INVARIANTS OF THE VELOCITY GRADIENT TENSOR

It has been seen that in curved pipes, as in the arterial system, the dominant topological features are vortical structures, which may increase mixing [13] and influence flow stability, however other forms of coherent structures are present in physiological conduits [39]. Vortices have been widely studied, however there is no converging approach as to the best way of defining them in 3D. Amongst the most used are the λ_2 criterion proposed by [40], the Q criterion proposed by [41], the Δ criterion [42] which are based on the velocity gradient tensor [40, 43], as well as other measures such as the helicity [44] and the vorticity. In this work we will observe the flow features using the velocity gradient tensor in describing the flow field due to the simplicity, elegance and detail of insight that can be obtained. The analysis remains local, however, such that time integrated effects and structures should be described by particle tracking or other means.

Let us consider a flow field free of singular cases such as shocks and vortex sheets. At an arbitrary point O in the flow field a Taylor series can be used to expand the velocity in terms of the spatial coordinate around O. This is equivalent to performing a perturbation of the

velocity field with respect to the spatial coordinates.

$$u_i = \dot{x}_i = A_i + A_{ij}x_j + A_{ijk}x_jx_k + \dots, \qquad i, j, k = 1, \dots, 3, \tag{4}$$

where A_{ij} is the velocity gradient tensor given by

$$\mathbf{A} = A_{ij} = (\nabla\mathbf{u}) = \frac{\partial u_i}{\partial x_j} = u_{ij}, \qquad i, j = 1, \dots, 3.$$

If the coordinate system is assumed to translate without rotation, with the origin following a passive particle trace, then the origin is a critical point location. In this frame of reference $A_i = 0$, and if O is on a no-slip boundary, then also $A_{ij} = 0$. In this work we will consider only the free-stream flow.

Truncating second and higher order terms in equation (4), a linear system of ODEs is obtained, hence $\dot{\mathbf{x}} = \mathbf{A} \cdot \mathbf{x}$, or explicitly

$$\begin{pmatrix} \dot{x}_1 \\ \dot{x}_2 \\ \dot{x}_3 \end{pmatrix} = \begin{pmatrix} u_{11} & u_{12} & u_{13} \\ u_{21} & u_{22} & u_{23} \\ u_{31} & u_{32} & u_{33} \end{pmatrix} \begin{pmatrix} x_1 \\ x_2 \\ x_3 \end{pmatrix}, \tag{5}$$

whose solution involves either real or imaginary eigenvalues (λ_i, $i = 1, \dots, 3$):

$$\begin{cases} x_1(t) &= x_1(0)e^{\lambda_1 t} \\ x_2(t) &= x_2(0)e^{\lambda_2 t} \\ x_3(t) &= x_3(0)e^{\lambda_3 t} \end{cases}, \qquad \begin{cases} x_1(t) &= x_1(0)e^{\lambda_1 t} \\ x_2(t) &= e^{\lambda_2 t}[x_2(0)\cos(\lambda_3 t) + x_3(0)\sin(\lambda_3 t)] \\ x_3(t) &= e^{\lambda_2 t}[x_3(0)\cos(\lambda_3 t) - x_2(0)\sin(\lambda_3 t)] \end{cases}. \tag{6}$$

These are the local instantaneous streamlines, hence describing locally the motion of the flow. In unsteady flow, the expansion in equation (4) is applied at a moment in time, such that the solution trajectories correspond to particle paths, which do not generally coincide with streamlines except at an instant.

For clarity we will order the eigenvalues such that, if they are all real then $\lambda_1 \geq \lambda_2 \geq \lambda_3$, while if the solution comprises of a real and complex conjugate pair then λ_1 is real and the complex conjugate pair is given by $\lambda_2 \pm i\lambda_3$. The eigenvectors indicate the principal directions of motion of the flow surrounding the critical point, hence they define the planes in which the solution locally osculates. In the case of three real eigenvalues, the solution trajectories osculate three distinct planes, while if the solution involves a complex eigenvalue, only one plane exists, given by the eigenvectors of the complex conjugate eigenvalues. In this case the plane defines the plane of rotation, while the eigenvector associated to the real eigenvalue indicates the local axis of swirling. It is important to note that the eigenvectors need not be orthogonal except in the case of irrotational flow.

For the case of an incompressible flow, the trace of the velocity gradient tensor is $tr(\mathbf{A}) = \partial u_1/\partial x_1 + \partial u_2/\partial x_2 + \partial u_3/\partial x_3 = 0 = \lambda_1 + \lambda_2 + \lambda_3$ (or if complex $= \lambda_1 + 2\lambda_2$). Thus, the sum of the eigenvectors is zero. Furthermore the ratio of the eigenvalues, if real will indicate the level of stretching and compressing of the flow along the eigenvectors, and if complex provide the spiralling compactness by λ_2/λ_3, since from equation (6) the time period of one revolution in the spiralling plane is given by $2\pi/\lambda_3$.

By tracking a passive particle path and plotting the associated eigenvectors, one can perceive the local dynamics surrounding the trajectory. In Figure 9 detail of a passive particle trajectory is shown in the region of a vortex structure such that there is a real and complex conjugate pair of eigenvalues. The plane of spiralling and its axis are shown at constant time intervals (0.002 s) along the trajectory.

Given eigenvalues $\lambda_1, \lambda_2, \lambda_3$ of the velocity gradient tensor $\mathbf{A} = \nabla\mathbf{u}$, the eigenvalue problem $[\mathbf{A} - \lambda_i I]e_i = 0$, $i = 1, \dots, n$, where e_i is the eigenvector associated to λ_i, can be determined solving the characteristic equation $\det[\mathbf{A} - \lambda_i I] = 0$, $i = 1, \dots, n$. For a 3×3 matrix as is our case, this can be written as

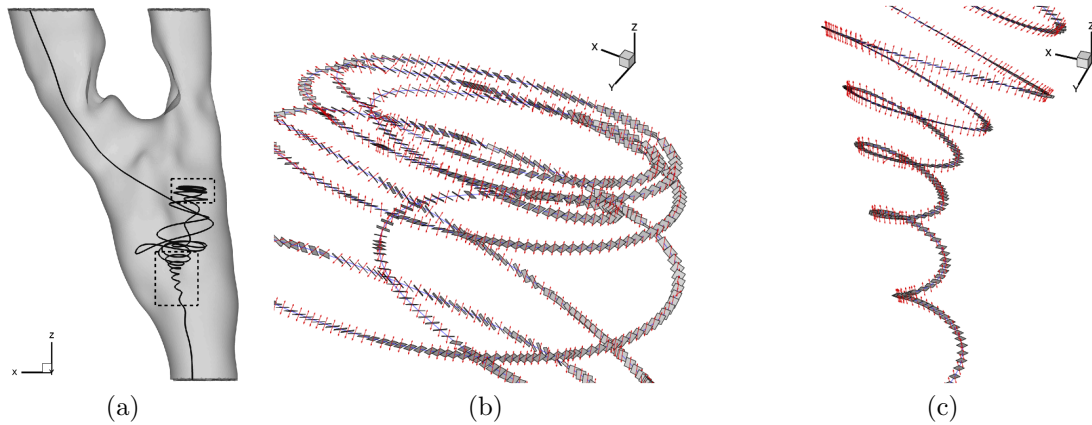$$\lambda_i^3 + P\lambda_i^2 + Q\lambda_i + R = 0, \qquad i = \dots, n,$$

Figure 9. (a) Graft and passive particle track and (b), (c) detail of the trajectory in a vortical structure where the solution is $\lambda_1, \lambda_2 \pm i\lambda_3$. Plane of swirling and axis of stretching are indicated, given by the eigenvectors of the velocity gradient tensor. It should be noted that for these details the foci are stable and $\lambda_1 > 0$.
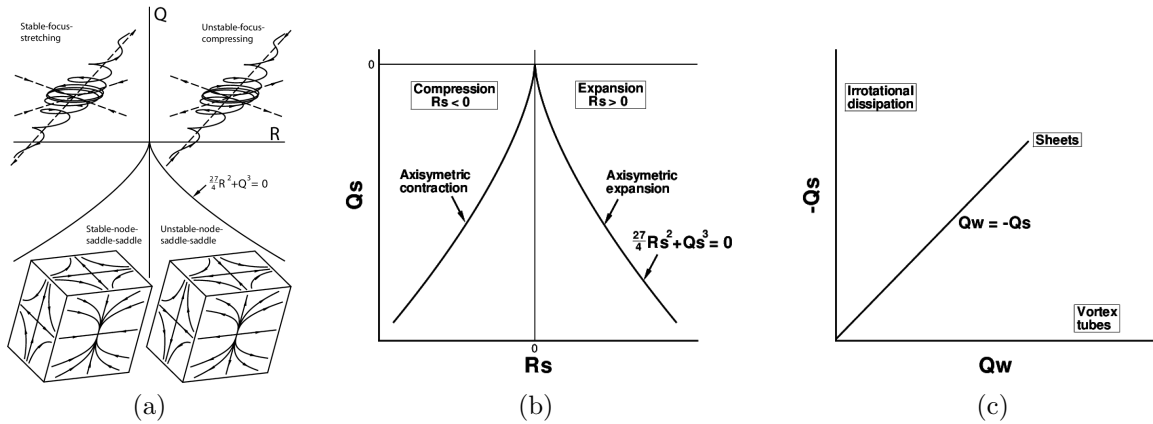

Figure 10. (a) Plot of the $Q - R$ plane at $P = 0$ showing the divisory line between real and complex solutions to the ODE system (5). (b) Plot of $R_s - Q_s$ plane and (c) of $-Q_s - Q_W$ plane and characteristic features of the fluid. In (a) the node-saddle-saddle configuration is obtained if the solution is given by three real eigenvalues, while a foci configuration if the solution consists in a real and a complex conjugate pair of eigenvalues.

where P, Q and R are the invariants

$$P = -(u_{11} + u_{22} + u_{33}) = -tr(\mathbf{A}),$$

$$Q = \begin{vmatrix} u_{11} & u_{12} \\ u_{21} & u_{22} \end{vmatrix} + \begin{vmatrix} u_{11} & u_{13} \\ u_{31} & u_{33} \end{vmatrix} + \begin{vmatrix} u_{22} & u_{23} \\ u_{32} & u_{33} \end{vmatrix}$$

$$R = \begin{vmatrix} u_{11} & u_{12} & u_{13} \\ u_{21} & u_{22} & u_{23} \\ u_{31} & u_{32} & u_{33} \end{vmatrix} = -\det[\mathbf{A}]$$

The surface that divides the real from complex solutions of the eigenvalues can be shown to be $27R^2 + (4P^3 - 18PQ)R + (4Q^3 - P^2Q^2) = 0$ [45]. For incompressible flow however $P = 0$ and the divisory line in the $Q - R$ plane becomes $\frac{27}{4}R^2 + Q^3 = 0$, as shown in Figure 10. In this way the invariants Q and R can be used directly in describing the flow field.
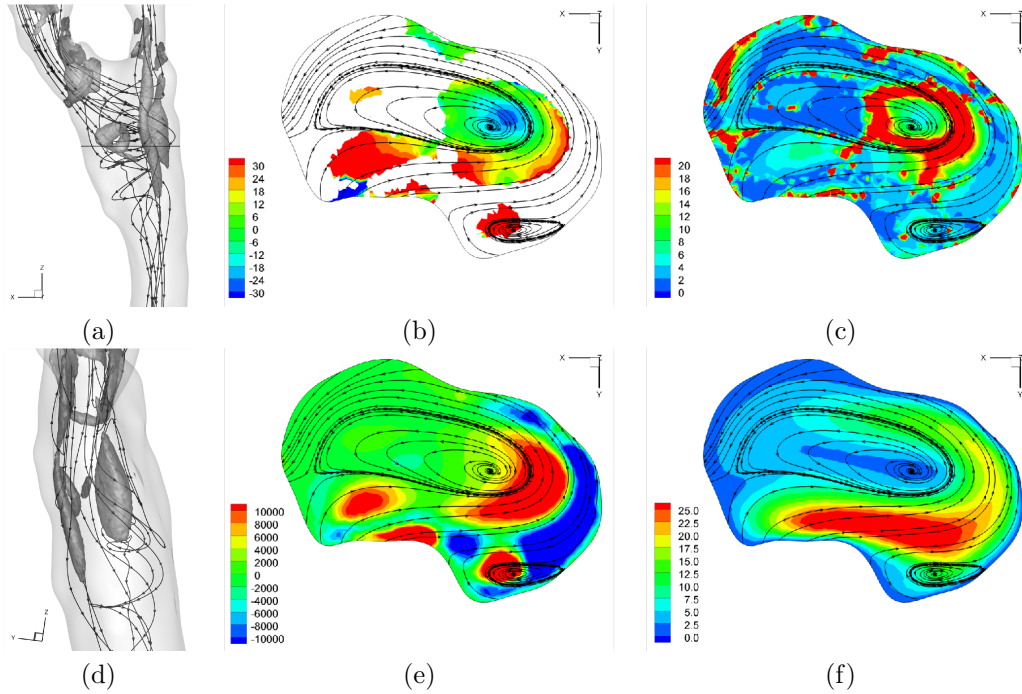
Figure 11. Result for G_O^{300} and Newtonian fluid. Passive particle track and iso-contours of Q=10000 viewed in-plane (a) and from the anastomosis 'floor' (d). Discernible is the jet from the graft that impinges on the anastomosis 'floor', which divides the flow due to the relative planarity of the vessel bifurcations to form two counter rotating vortices. Cross section (location shown in (a)) of: (b) magnitude of λ_1 for complex eigenvalues of the velocity gradient tensor (regions where the eigenvalues are all real a coloured white); (c) $|\lambda_3/\lambda_2|$ to indicate the spiralling compactness (for a foci configuration as indicated for regions shown in (b)); (e) Q (the second invariant of the velocity gradient tensor) (f) velocity magnitude (m s^{-1}).

The velocity gradient tensor can be split into a symmetric and antisymmetric part, corresponding to rate-of-strain and rate-of-rotation tensors, hence $\nabla \mathbf{u} = \partial u_i/\partial x_j = S_{ij} + W_{ij}$, $i, j = 1, \ldots, 3$, where $S_{ij} = (\partial u_i/\partial x_j + \partial u_j/\partial x_i)/2$ and $W_{ij} = (\partial u_i/\partial x_j - \partial u_j/\partial x_i)/2$. Following the analysis above, the invariants of S_{ij} are Q_S and R_S, while the invariant of W_{ij} is Q_W, noticing that P, P_S, P_W and $R_W = 0$ for an incompressible flow. Physical meaning to these invariants is briefly given as follows [46]: $Q = Q_S + Q_W$ is a measure of the rate of rotation over strain rate; $Q_S \propto$ rate of viscous dissipation of kinetic energy, $Q_W \propto$ vorticity intensity, positive R_S is associated with sheetlike structures, and negative R_S to tubelike structures. Indicative plots are given in Figure 10. These invariants are widely used in the study of fluid mechanics [46].

Using the above, the flow field can be studied and interpreted accordingly. In Figure 11 the core flow is studied by taking iso-contours of Q and observing passive particle trajectories with respect to these. It is evident that two counter rotating vortices are set up along the 'floor' of the anastomosis, as also detailed in [11, 10]. The gross flow characteristics are seen to be a jet forming from the graft stenosis, that impinges on the anastomosis 'floor' setting up two counter rotating vortices, and forms regions of recirculating flow at the anastomosis 'toe' and 'heel'. A cross section of the domain is shown with different measures and the in-plane particle paths. The regions of high values of Q are not coincident with the spiralling flow core, while the $|\lambda_3/\lambda_2|$ show a greater correlation, demonstrating that there is a higher spiralling compactness around the approximate vortex core. Furthermore the value of λ_1 in the region where the eigenvalues are complex (regions where the solution is real appear white)
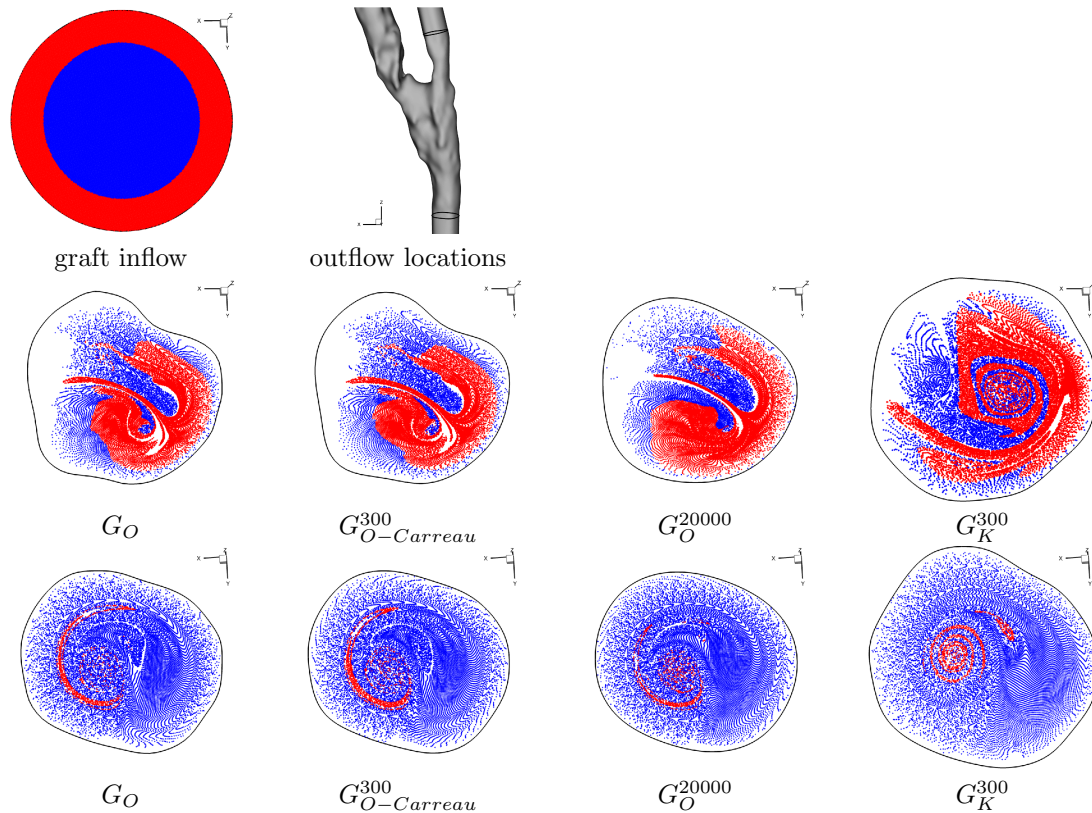
Figure 12. Inflow (top row) and outflow (middle row: proximal; bottom row: distal) cross sections, showing the particle distributions of the two equally numbered species. Location of common outflow cross sections are indicated in the top-right image.

tend to agree with the information provided by $|\lambda_3/\lambda_2|$, indicating a bigger stretching in the approximate region of the vortex core which is a region of low spiralling compactness.

6. ENTROPIC MEASURE OF MIXING

In this section we describe how the mixing is computed through an entropic measure with a new improved resolution. The mixing is calculated by tracing passive particles from the graft inflow to the proximal and distal outflows and comparing the particle distributions at these cross sections, thus observing the cumulative effect of the flow structures the particles traverse. The results for examples of the cases studied are shown in Figure 12, where the particles are divided into distinct species of equal number, based on their distance from the wall at the inflow cross section. This is done to study the effect of exchange processes between the near-wall region and the core flow, which are of known importance in physiology. The particles are uniformly seeded at the inflow section, however other forms of initial particle profile can be used based for example on the local mass flux or velocity field [47], that may result more physiologically representative or more appropriate in studies of particle deposition. For steady state passive particle tracking, giving equal importance to each particle in the mixing analysis, the initial distribution only influences the resolution and a densly populated Cartesian grid is used here.

Mixing is of importance in physiological flows in several aspects, for example in blood flow poor mixing is linked to disease formation such as atherosclerosis [13], in nasal airflows mixing

is of importance to permit good humidity and thermal exchange, and also in the lungs mixing and deposition are of marked interest [48]. Mixing properties are also related to the delivery of drugs, oxygen and other substances in the body.

Mixing by a flow is the consequence of *stirring* and *diffusion* [49, 50, 51]. Stirring is the result of advection and can be considered the mechanical stretching and folding of material interfaces, while diffusion permits mixing across interfaces. Let us consider the non-dimensional advection-diffusion equation

$$\theta_t + \mathbf{u} \cdot \nabla\theta = Pe^{-1}\nabla^2\theta. \tag{7}$$

where θ is the solute concentration. For large Péclet number, Pe, as is usually the case in blood flow in arteries, the advective term is dominant and efficient mixing is achieved by increasing interface lengths and decreasing striation thickness that permit a greater diffusion of different species to occur. In this work we will look only at the stirring, in specific the cumulative effect of the flow structures in the anastomosis by means of advection solely.

The measure of mixing is calculated based on the entropy in that it describes the probability of the location of particles. The Shannon entropy is a measure of lack of information such that the higher the information dimension, the more random the system is and the less information it can convey [52]. The method presented here is a development of that presented in [53] for the study of chaotic micromixers. Similar works include [52] for polymer processing using the Renyi entropy, while other works using the Shannon entropy include [54] for a single screw extruder, [13] for a helical pipe, [56] for the right coronary artery and [55] for nasal cavities.

In this work two developments are proposed to extend the standard method. Firstly the notion of cross section division into cells for 'box counting' is replaced by a nearest neighbourhood search of particles. Secondly the mixing measure of relative entropy is extended to the case of multiple inflow/outflow sections. The standard method is first presented and discussed in detail, followed by description of the developments which resolve some pitfalls and increase the resolution of the analysis.

In the above mentioned 'box counting' methods N_p particle tracks for N_s different species of equal quantity are initially computed. Then a cross section is extracted where the mesure of mixing is sought. The cross-sectional area A at this location of interest is divided into small equally sized N_c cells of area A_c as given by a mesh, such that the total area of the section is $A = N_cA_c$. The entropy H is given by

$$H = -\sum_{i=1}^{N_c}\left(w_i\sum_{j=1}^{N_s}(p_{i,j}\mathrm{ln}p_{i,j})\right) \tag{8}$$

where i is the index for the cells, j is the index for the particle species, N_c is the number of cells, N_s is the number of species, $p_{i,j}$ is the particle number fraction of the jth species in the ith cell, and w_i is the weight such that $w_i = 0$ if the cell is empty or contains only one species and $w_i = 1$ otherwise. Hence $p_{i,j}$ can be thought of as the joint probability for a particle to be of species j in cell i, where all particles (irrespective of species) are considered in formulating the probability. Therefore $\sum_{i=1}^{N_c}\sum_{j=1}^{N_s}p_{i,j} = 1$. Other 'box counting' methods such as those presented in [57, 58, 49] give a different interpretation to the particle distributions, depending on the details of the method and measures sought, some of which are compared in [59].

A number of parameters need to be selected. In [52] changes of N_s, N_c and N_s are studied to see what effect they have on the entropy. The calculated entropy is fairly insensitive to changes in N_c and N_s, even though $N_p \gg N_c \gg N_s$ using a ratio of $N_p = N_sN_c$. It is clear that as the area of the cells increases, *i.e.* $N_c \to 0$, the entropy reaches maximum value. Conversely, if $N_c \to \infty$, then $H \to 0$. In the study of efficiency of mixers [52], tests have been performed for $O(700)$, $O(6,000)$ and $O(11,000)$ particles to show that similar results are obtained and the measure of entropy calculated in this way is largely insensitive and convergent for large N_p. In [56] mixing in the right coronary artery $N_p = O(40,000)$, $N_c = O(10,000)$ and $N_s = 2$ are used with confidence that there are sufficiently large numbers of particles and cells to avoid considerations of errors due to this discrete method. However [13] indicate the need for

$N_p = O(60,000)$ and $N_c = O(10,000)$. From a statistical standing, for a perfectly randomised population of particles the Poisson distribution describes the probability, relating the number of cells to the expected number of particles to lie therein [49], leading to a informed approach of choosing cell number. In practice the ratio of particle number and cell size reflects the desired mixing scale (or grain), related to the average striation thickness, to be studied.

Moreover the cell size to cross-sectional area ratio (A_c/A) is important since the smaller the cells the higher the resolution of the analysis performed. The area ratio, and hence the number of cells, is kept constant for all cross-sections to ensure that the relative probability of a particle being in a cell is unchanged. Furthermore the aspect ratio of the cells should be kept as small as possible to ensure that particles within a cell are not in fact far apart.

Finally, the absolute value of H is difficult to relate to directly and is therefore normalised to the maximum possible mixing. Let us define H_0 as the mixing entropy at the location the particles are initially released. Then, H_0 is an initial state and should correspond to the minimum entropy. We also define H_{max} as the maximum possible mixing entropy, given by $H_{max} = \ln(N_s N_c) = \ln(N_s A/A_c)$. This can be obtained by choosing $p_{i,j} = 1/(N_c N_s)$ for all particles and cells, hence absence of any information about the system, i.e. complete disorder. Therefore $H_0 \leq H \leq H_{max}$. The degree of mixing κ is defined [53] as

$$\kappa = \frac{H - H_0}{H_{max} - H_0} \tag{9}$$

The value $\kappa = 1$ corresponds to a uniform particle distribution. It would be expected that as further downstream one goes, the greater κ becomes, until it will tend to level off. The above discussion details the standard method.

The approach is based on cells to calculate the entropy and it requires care to ensure that the result is independent of the cell number and shape. To overcome this one tends to use a large amount of particles and cells where $N_p \geq N_s N_c$, hence errors associated with the method will reduce to being insignificant, though it will require large amounts of computation. Furthermore, the limitation to binning particles into cells removes the information that may be present in neighbouring cells. For example, two particles at very small distance from each other may lie in two different cells and the relationship to each other lost. Division of the cross-section into cells is also sensitive to their aspect ratio and cell area, which may locally vary if the cross-section is of complex shape. To avoid the dependency on cells we propose a new binning method based on the radius of influence r from the particles. Equation (8) now becomes

$$H = -\sum_{i=1}^{N_p} \left(\frac{w_i}{n_i} \sum_{j=1}^{N_s} p_{i,j} \ln p_{i,j} \right)$$

where n_i is the number of particles within support radius r from the interrogation particle. Division by n_i is required to give this particle an equal weighting since it lies within the radius of other n_i particles and will therefore be considered a total of n_i times. When a particle is close to the wall, part of the region of influence lies outside the domain. To correct this bias so that all particles have the same effective influence, r is increased accordingly to ensure that a constant area is covered within the fluid cross section.

Given that the area of the bins is given by $A_b = \pi r^2$, then the value of the maximum entropy now becomes $H_{max} = \ln(N_s A/A_b)$, where the ratio of A/A_b should be maintained for all cross sections. Now if we consider the case of the bypass geometry where the mass outflow split is 40% proximal and 60% distal, then this split should also be maintained with respect to bin size:

$$\frac{A_{proximal}}{A_{b\ proximal}} = 0.4 \frac{A_{graft}}{A_{b\ graft}}, \qquad \text{and} \qquad \frac{A_{distal}}{A_{b\ distal}} = 0.6 \frac{A_{graft}}{A_{b\ graft}},$$

where A_{graft}, $A_{proximal}$ and A_{distal} are the cross-sectional areas of the graft, proximal and distal vessels, respectively, while $A_{b\ graft}$, $A_{b\ proximal}$ and $A_{b\ distal}$ are the bin areas for the graft, proximal and distal vessels, respectively. The entropy at the outflow sections are therefore

summed to give $H = H_{proximal} + H_{distal}$ in equation (9), and results are presented in Table II.

Similarly as for the scheme based on cells, the method performs well if the number of particles and radius of the bins are given by $N_p \geq N_s A/A_b$. By removing the meshing of the cross-sectional area and defining the neighbourhood based on the support radius instead, the accuracy of the mixing for a reduced number of particles is increased.

As noted in [53, 56], particles that get close to the wall are 'lost' or 'stuck' due to the low velocities present in these regions, hence never feasibly making it to the cross-section location of interest, as also seen in Figure 12. The majority of the particles are lost in the initial stages of the tracking due to the release of these particles close to the wall. Therefore the particles that get stuck at the start are omitted from the calculations. In this work, in the most extreme cases found, the number of particles that fail to pass through the domain in a feasible time (10 s) is $O(2,000)$ particles for an initial seeding of $O(40,000)$ particles, hence a 5% error.

Given that the tracer particles are studied as passive and the flow is steady, it is important to note that the entropy calculated is related to the length of interface that divides the species, as indicated in [57]. Furthermore it should be noted that while the number of particles N_p and area of bins A_b are sought to be independent of the method, so as to achieve a convergence of the relative entropy, comparison with different cases and geometries is only valid if the number of particles, their initial configuration and support radius are maintained.

A word of warning as regards to the level of detail is in order when inferring the relation between the entropy measured and the length of interface between species, since it depends greatly on the resolution studied. In [59] noticeable error is reported despite the large number of particles used ($O(10,000)$), since the measure of relative entropy obtained describes the striation thickness and stretching only to the resolution of the number of particles and cells used. Therefore, if fine detail is expected then the number of particles should increase and their support radius decrease. The result is that the choice of the number of cells and particles should be evaluated depending on each case studied individually, bearing in mind the expected size of detail or parameters such as the Péclet number. In this work the number of particles is $N_p = O(40,000)$, number of species $N_s = 2$, the expected particle density (for uniform particle distribution) $\rho = 10$, and the area ratio $A/A_b = 4,000$, making the radius of influence at the graft inflow cross section $r \approx 0.035$ mm.

7. RESULTS COMPARING THE DIFFERENT CASES

In this section results are presented comparing effects of uncertainty with respect to the resulting flow solution. Uncertainty considered includes using two different segmentation methods (Otsu and Kittler), three different levels of smoothing (none, 300 and 20000 iteration steps), and two different fluid models (Newtonian and Carreau generalised Newtonian). Specific examples that describe well the trends observed are discussed in greater depth.

Comparing both quantitatively as well as qualitatively the flow field is intricate. An approach is to observe the vortical structures. This is done here by identifying iso-contours of high Q (second invariant of the velocity gradient tensor), shown in Figure 13. In this figure the pair of counter-rotating vortices along the 'floor' of the anastomosis are evident, as are other structures which on closer observation are regions where the flow is locally curving but not part of vortical strucutres.

Rheological model	G_K	G_K^{300}	G_K^{20000}	G_O	G_O^{300}	G_O^{20000}
Newtonian	0.34	0.35	0.26	0.27	0.26	0.25
non-Newtonian	0.33	0.34	0.25	0.26	0.25	0.24

Table II. Relative mixing at the distal and proximal vessels, with respect to the bypass graft inflow, for cross sections shown in Figure 1. Indicative particle track cross sections are shown in Figure 12.
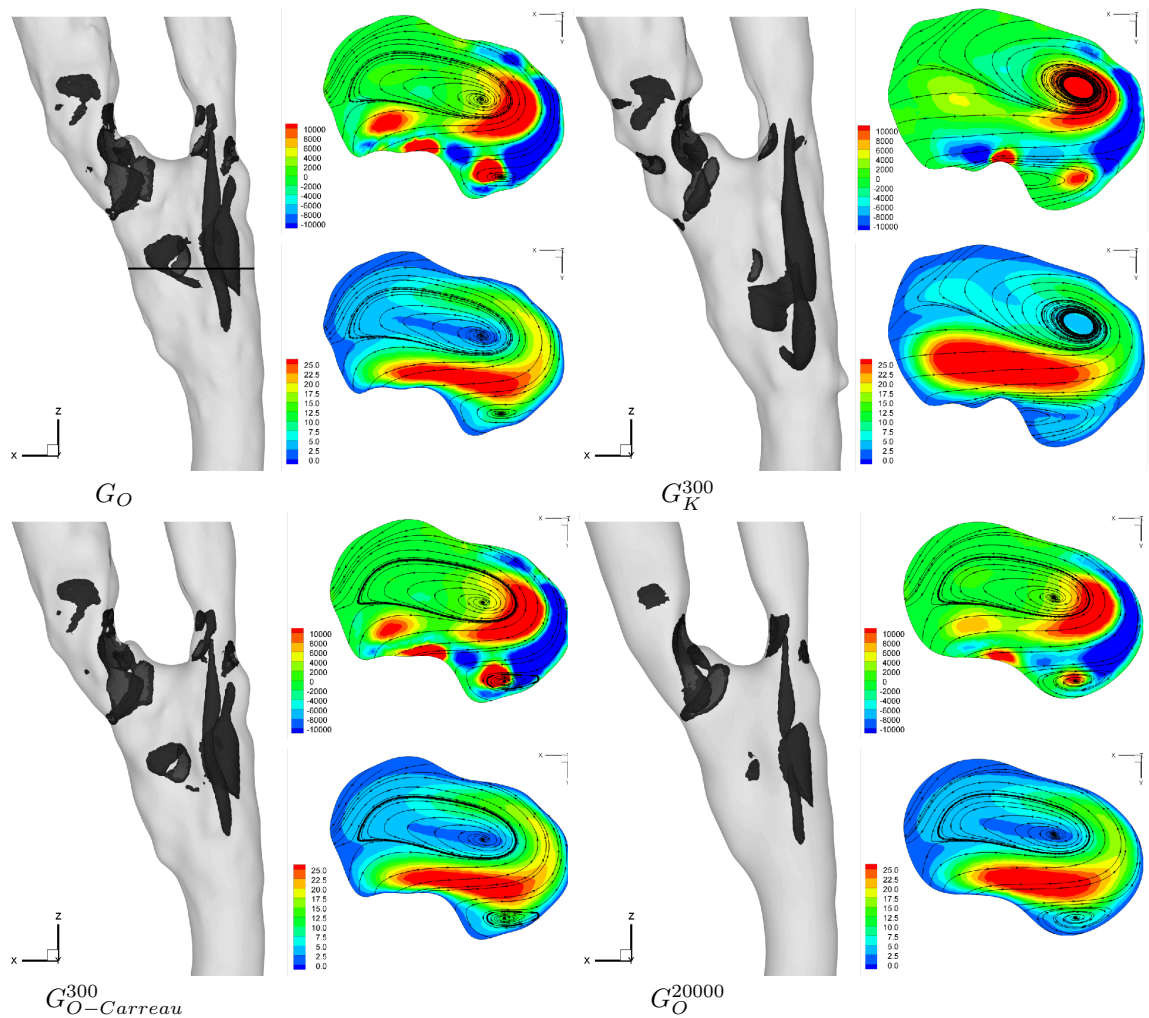
G_O

G_K^{300}

$G_{O-Carreau}^{300}$

G_O^{20000}

Figure 13. Q=10000 iso-surfaces and cross sections showing Q (top), the velocity magnitude (m s^{-1}) (bottom) and in plane particle trajectories, for a selection of the cases studied. Top left insert shows the cross section location.

It is apparent that as the geometry becomes smoother due to the more intense surface smoothing, the vortical structures become less pronounced. There is little difference between the Newtonian, non-Newtonian, and moderate surface smoothing, as seen when comparing G_O and $G_{O-Carreau}^{300}$. Differences in the vortical structures are more pronounced when comparing results obtained using different segmentation methods. These results are made clearer by observing the cross section of Q as well as the velocity magnitude, also shown in Figure 13. These sections are approximately at the same height as the region of impingement of the flow on the anastomosis 'floor', and also cut into the reversed flow region at the 'toe' of the anastomosis. The in-plane particle trajectories indicate a greater influence of a vortical structure in the case of the Kittler segmentation, with larger regions of faster moving fluid showing the wrapping around of the flow. These indicate that the increased vessel patency facilitates the formation of vortical structures.

In Figure 14 the wall shear stress (WSS) magnitude and the surface shear lines (SSL) are presented. The latter are obtained by integrating the WSS components along the surface and indicate the near-wall flow direction. Observing the complex patterns of the WSS and the SSL, the region of flow impingement is visible on the anastomosis 'floor' and separated flow
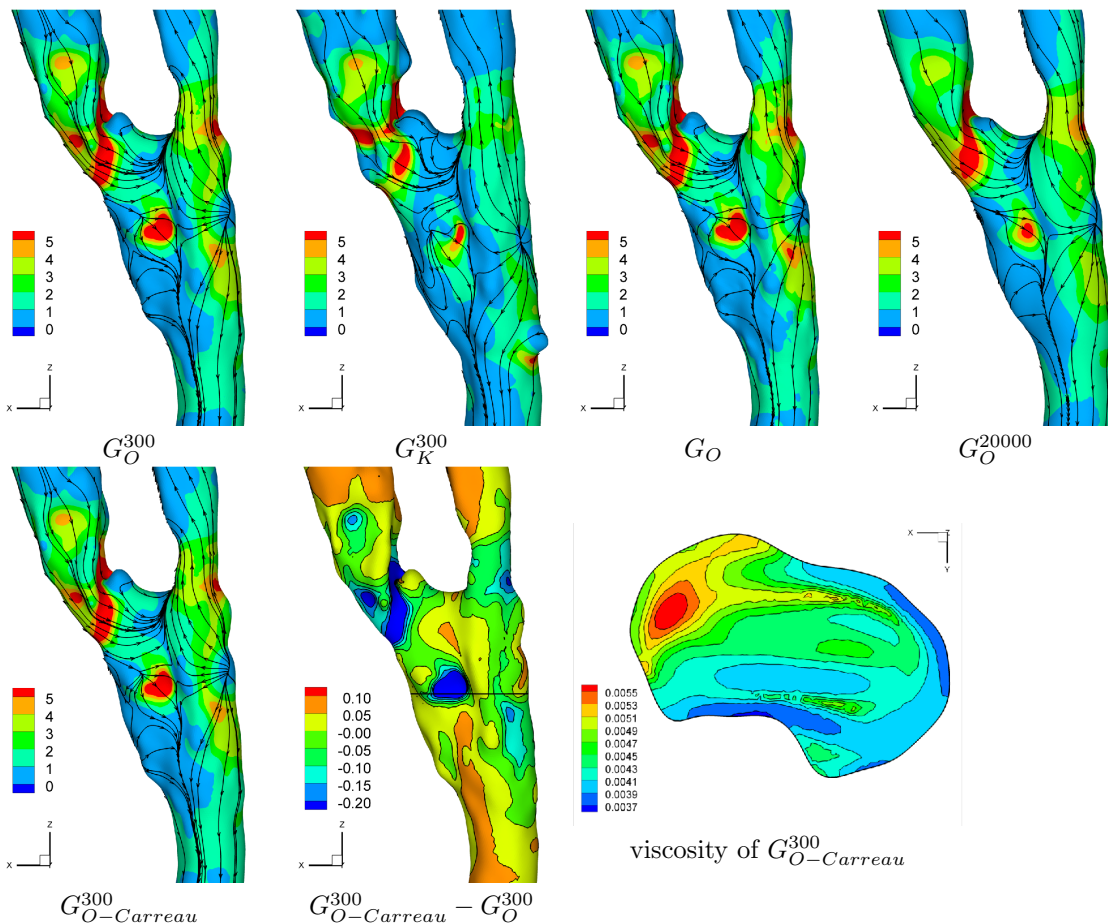
Figure 14. Wall shear stress (Pa) and surface shear lines (as the integrated path of the wall shear stress components). The wall shear stress difference in the non-Newtonian and Newtonian computations result in little change as shown by $G^{300}_{O-Carreau} - G^{300}_{O}$. A cross section of the apparent viscosity (Pa s) obtained from a non-Newtonian simulation is shown.

regions at the anastomosis 'toe' and 'heel' are also discernible. From the SSL one can also notice the effects of the vortical structures. The influence of the surface smoothing is evident as a reduction of the complex patterns of WSS. The effect of use of different segmentation is apparently not so pronounced, and the SSL patterns are comparable between the cases despite the apparent difference in the core flow field. However, the stagnation point is seen to shift and the values of WSS magnitude locally also vary noticeably.

The effect of the rheological model is again seen to have a lesser impact on the flow than uncertainties in the virtual model surface definition. The difference, shown in Figure 14($G^{300}_{O-Carreau} - G^{300}_{O}$), indicates that the WSS difference is of the order of 0.1 Pa. This aspect is important when observing regions of low WSS that is widely accepted to be associated to disease in arteries, as at the anastomosis 'toe', where the Newtonian model yielding a good approximation but underestimates WSS.

While the Carreau non-Newtonian model used is obtained from experimental *in vitro* data, the value for the Newtonian model should be an approximation to this for the case studied. In this work a value of $\mu = 0.004$ Pa s was used in all the simulations. A further set of Newtonian simulations were performed to study the sensitivity of this choice and values of $\mu = 0.0035$ and $\mu = 0.0046$ Pa s were used, the latter being the average viscosity over the domain for the $G_{O-Carreau}$ simulation, while the prior is commonly used in the study of the arterial system
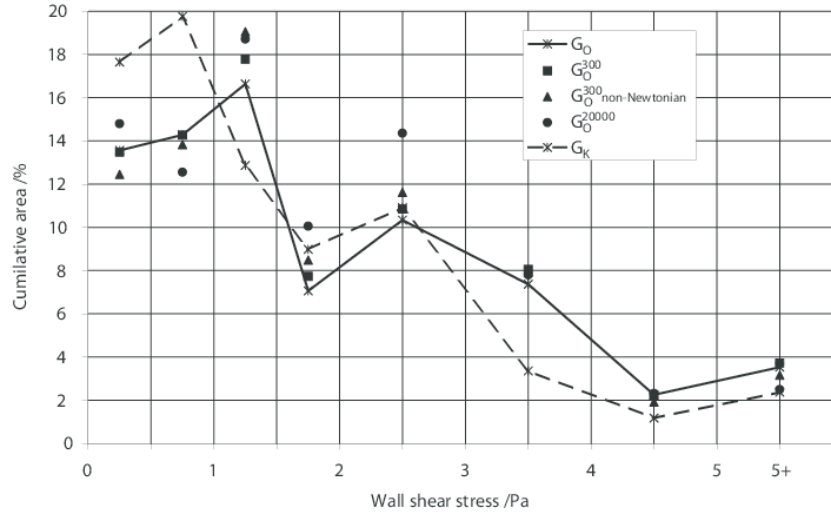
Figure 15. Cumulative area distribution for the wall shear stress for ranges 0-0.5, 0.5-1.0, 1.0-1.5, 1.5-2.0, 2.0-3.0, 3.0-4.0, 4.0-5.0 and 5.0+. Representative uncertainty is shown, due to difference in: thresholding, surface smoothing and rheological model. Greatest discrepancies in regimes of low wall shear stress are due to image segmentation uncertainty.

[60, 61]. It should be noted that the lowest viscosity seen from the $G_{O-Carreau}$ simulation was approximately $\mu = 0.0036$ Pa s. The WSS and SSL patterns are very similar, however on average choosing $\mu = 0.004$ Pa s gives closer results to the Carreau model used. The difference in WSS between the use of $\mu = 0.004$ and $\mu = 0.0035$ or $\mu = 0.0046$ Pa s is on average 0.13 and 0.15 Pa respectively. The greatest differences between these Newtonian models are seen at the stenosed regions of the graft and proximal artery (at the junction with the anastomosis) and the location of the stagnation point on the anastomosis 'floor' (which shifts by approximately 0.15 mm). In these regions only, the differences in WSS are on average 0.38 and 0.41 Pa between the use of $\mu = 0.004$ and $\mu = 0.0035$ or $\mu = 0.0046$ Pa s, respectively.

By observing the values of mixing, as an integrated effect of the flow field, the values are approximately constant as shown in Table II, however there are some noticeable differences in the particle track cross sections presented in Figure 12. The largest common difference is obtained by use of a different segmentation method, where the values range from $\kappa = 0.35$ to $\kappa = 0.25$. The increase in smoothing tends to reduce the mixing possibly by the reduced strength of the vortical structures to give rise to a less striated configuration. We observe that if a different initial configuration of particle species at the graft inflow is given in order to observe different phenomena, instead of concentric as presented here, the relative mixing of the species may be different. From the particle path cross sections presented in Figure 12, most of the faster moving flow at the inlet will exit through the distal vessel, and conversely a greater portion of the slower moving flow will exit the proximal vessel.

To quantify the uncertainty, or error, associated with performing numerical studies based on patient specific *in vivo* measurements with relation to the WSS, a probability density function can be formulated and presented as a percentage area associated to ranges of WSS. Results for the sample cases is shown in Figure 15. As mentioned above, and seen in this plot, the effect of the non-Newtonian model is to reduce peaks in very high or low WSS. Most of the error bounds in the WSS probability density function are within 5% surface area, or proportionally $\sim 40\%$ surface area. The largest errors in the region of low WSS are primarily seen due to the segmentation. Nevertheless, the remaining factors of uncertainty studied here also give large discrepancies in other ranges of WSS. The factor of scaling, due to the difference in Reynolds

number between the Kittler and Otsu families of virtual models, was given to be in the order of 10% and the results presented indicate a larger disagreement.

The effect of the change in geometry definition and the rheological models used can also be measured in terms of the pressure drop across the domain. While not a sensitive measure locally, the overall change can give an appreciation of the study parameters. It has been found that a pressure drop from graft inflow to distal outflow was of the order of 100 Pa for the Otsu segmentations and 75 Pa for the Kittler segmentations, and from the graft inflow to the proximal outflow the pressure drops were approximately 75 Pa and 55 Pa, respectively, which is a greater difference than given by considering the hydraulic diameter. The effect of smoothing is to decrease these magnitudes by around 3 Pa and 10 Pa from the original to the smoothed cases, using 300 and 20000 iteration steps, respectively. The effect of non-Newtonian modelling is not emphatic, with increased pressure drops in the order of 1 Pa with respect to the Newtonian case using $\mu = 0.004$ Pa s.

8. CONCLUSION

This work presents a patient specific study of uncertainty in the computed steady state flow solution for a peripheral bypass graft, with respect to geometry definition and constitutive model of blood. The topological uncertainty is introduced as different methods of automatic segmentation of the medical images and varying intensities of surface smoothing of the reconstructed virtual models. Newtonian or generalised Newtonian Carreau models are used to observe the uncertainty associated with describing the rheological behaviour of blood. The methods presented are automatic for the greatest part, relying only on minimal user intervention and permitting for a relatively fast turn around time and user independence.

Methods to derive quantitative and qualitative comparisons in the flow field are presented and related to clinical relevance; in specific the wall shear stress, velocity gradient tensor and mixing are used as key measures. Novel enhancements in the method of calculating the mixing permit an increased resolution in the analysis and the possibility of coping with split cross sections. Description of the segmentation, reconstruction and smoothing methods are also discussed, including analysis of the variability in the virtual model definition that arise.

Uncertainty in the virtual model definition due to the different segmentation methods was on average under 1 pixel, but locally as large as 4 pixels. The surface smoothing was found to yield a faithful representation to the medical image data if moderate (using 300 iterations), retaining the local features while removing reconstruction artefacts. More pronounced smoothing (using 20000 iterations) yielded geometries with reduced detail that could be considered as idealisations, that while not entirely matching the medical image data captured many details. Both different segmentations and levels of smoothing preseved the bifurcation angles of the vessels, using the discrete method following [1]; furthermore the volume and surface area are not preserved nor their ratio maintained in the case where the segmetnation method is different.

Uncertainty bounds associated to WSS, as presented in Figure 15 as a probability density function, indicate errors of 5%, and proportional errors in the order of 40%. Differences in the mixing are also in the order of 50%. It is found that on the whole the largest discrepancies in the flow field are given by the use of different medical image segmentation methods and surface smoothing, affecting especially the percentage of anastomosis subjected to low values of WSS and the levels of mixing with clear healthcare implications. Vortical structures are seen to be less strong for smoothed geometries and with the Otsu segmetnation (which has a reduced patency with respect ot the Kittler segmentation), resulting also in reduce mixing values.

For the case studied, the mixing, vortical structures and pressure drop are not as greatly influenced by the rheological model used compared to the variablility in the segmentation or smoothing intesity. Furthermore, the WSS patters and magnitudes for the case studied also indicate that a Newtonian model can yield a good approximation to the Carreau model, if the

viscosity value is carefully chosen. However, it is important to emphasise that the use of non-Newtonian models in medical applications is prevalent where WSS is commonly correlated to healthcare, since the Newtonian assumption under-estimates the low WSS regions, as shown in Figures 14 and 15. While non-Newtonian modelling is known to be important especially in the cases with a range of low shear rates, which are present for the geometry configuration and flow rates used in this study, these effects are secondary to the geometrical uncertainty. In order to quantifying the general relative importance of the geometric and modelling uncertainties, further studies that encapsulate a wider range of geometries are necessary.

In fact, this work develops a number of aspects to incorporate uncertainty, however the analysis presented is by no means complete, while still identifying problematic aspects in the numerical modelling of *in vivo* patient specific data. To achieve a more accurate range of the errors, a further array of segmentation methods could be analysed. Also, different non-Newtonian models should be studied and compared. While alternative generalised Newtonian models are expected to behave in a similar way to the Carreau model, other non-Newtonian properties such as yield stress, thixotropy and viscoelasticity should be studied regarding the uncertainty in the choice of the fluid model for blood. Furthermore, the analysis should be extended to unsteady simulations and the effect of the boundary conditions, performing these in a combinatorial manner.

9. ACKNOWLEDGEMENTS

REFERENCES

1. Gambaruto AM, Peiró J, Doorly DJ, Radaelli AG. Reconstruction of shape and its effect on flow in arterial conduits. *International Journal for Numerical Methods in Fluids* 2008; **57**(5):495–517.
2. Sezgin M, Sankur B. Survey over image thresholding techniques and quantitative performance evaluation. *Journal of Electronic Imaging* 2004; **13**(1):146–165.
3. Gambaruto AM, Taylor DJ, Doorly DJ. Modelling nasal airflow using a Fourier descriptor representation of geometry. *International Journal for Numerical Methods in Fluids* 2009; **59**(11):1259–1283.
4. Robertson A, Sequeira A, Kameneva M. Hemorheology. *In: Haemodynamical Flows: Modelling Analysis and Simulation. G. P. Galdi, R. Rannacher, A. Robertson and S. Turek eds* 2008; pp. 63–120.
5. Robertson MA, Sequeira A, Owens R. Rheological models for blood. *In: Cardiovascular Mathematics. Modeling and simulation of the circulatory system. Formaggia, L., Quarteroni, A. M., Veneziani, A., eds. Series: MS, Springer* 2009; **1**: pp. 213–244.
6. Anand M, Rajagopal KR. A shear-thinning viscoelastic fluid model for describing the flow of blood. *International Journal of Cardiovascular Medicine and Science* 2004; **4**(2):59–68.
7. Shimogonya Y, Ishikawa T, Imai Y, Matsuki N, Yamaguchi T. Can temporal fluctuation in spatial wall shear stress gradient initiate a cerebral aneurysm? A proposed novel hemodynamic index, the gradient oscillatory number (GON). *Journal of Biomechanics* 2009; **42**(4):550–554.
8. Ku DN, Giddens DP, Zarins CK, Glagov S. Pulsatile flow and atherosclerosis in the human carotid bifurcation. *Arteriosclerosis* 1985; **5**(3):293–302.
9. Caro CG, Doorly DJ, Tarnawski M, Scott KT, Long Q, Dumoulin CL. Non-Planar Curvature and Branching of Arteries and Non-Planar-Type Flow. *Proceedings: Mathematical, Physical and Engineering Sciences* 1996; **452**(1944):185–197.
10. Doorly DJ, Sherwin SJ, Franke PT, Peiró J. Vortical Flow Structure Identification and Flow Transport in Arteries. *Computer Methods in Biomechanics and Biomedical Engineering* 2002; **5**(3):261–275.
11. Sherwin SJ, Shah O, Doorly DJ, Peiró J, Papaharilaou Y, Watkins N, Caro CG, Dumoulin CL. The Influence of Out-of-Plane Geometry on the Flow Within a Distal End-to-Side Anastomosis. *Journal of Biomechanical Engineering* 2002; **122**(1):86–95.
12. Giordana S, Sherwin SJ, Peiró J, Doorly DJ, Papaharilaou Y, Caro CG, Watkins N, Cheshire N, Jackson M, Bicknall C, Zervas V. Automated classification of peripheral distal by-pass geometries reconstructed from medical data. *Journal of Biomechanics* 2004; **38**(1):47–62.
13. Cookson AN, Doorly DJ, Sherwin SJ. Mixing through stirring of steady flow in small amplitude helical tubes. *Annals of Biomedical Engineering* 2009; **17**(4):710–721.

14. Lee KE, Parker KH, Caro CG, Sherwin SJ. The spectral/hp element modelling of steady flow in non-planar double bends. *International Journal for Numerical Methods in Fluids* 2008; **57**(5):519–529.
15. Castro MA, Putman CM, Cebral JR. Computational fluid dynamics modeling of intracranial aneurysms: effects of parent artery segmentation on intra-aneurysmal hemodynamics. *Americal Journal of Neuroradiology* 2006; **27**(8):1703–09.
16. Moore JA, Steinman DA, Ethier CR. Computational blood flow modeling: errors associated with reconstructing finite element models from magnetic resonance images. *Journal of Biomechanics* 1998; **31**(2):179–184.
17. Glor FP, Long Q, Hughes AD, Augst AD, Ariff B, McG Tham SA, Verdonck PR, Xu XY. Reproducibility study of magnetic resonance image-based computational fluid dynamics prediction of carotid bifurcation flow. *Annals of Biomedical Engineering* 2003; **31**(2):142–151.
18. Lee SW, Steinman DA. On the relative importance of rheology for image-based CFD models of the carotid bifurcation. *Journal of Biomechanical Engineering, Technical Briefs* 2007; **129**(2):273–278.
19. Johnston BM, Johnston PR, Corney S, Kilpatrick D. Non-Newtonian blood flow in human right coronary arteries: transient simulations. Journal of Biomechanics, 2006, 39(6):1116–1128.
20. Johnston BM, Johnston PR, Corney S, Kilpatrick D. Non-Newtonian blood flow in human right coronary arteries: steady state simulations. Journal of Biomechanics, 2004, 37(5):709–720.
21. Bodnar T, Sequeira A. Numerical Study of the Significance of the Non-Newtonian Nature of Blood in Steady Flow Through a Stenosed Vessel. *In: Advances in Mathematical Fluid Mechanics, Springer, Berlin and Heidelberg* 2009; pp. 83–104.
22. Sequeira A, Janela J. A note on computational blood rheology. *in PAMM-Proceedings of Applied Mathematical Mechanics* 2007; **7**: 1101207–1101208.
23. Lee KL, Doorly DJ, Firmin DN. Numerical simulations of phase contrast velocity mapping of complex flows in an anatomically realistic bypass graft geometry. *Medical Physics* 2006; **33**(7):2621–2631.
24. Giordana S, Sherwin SJ, Peiró J, Doorly DJ, Crane JS, Lee KE, Cheshire NJ, Caro CG. Local and global geometric influence on steady flow in distal anastomoses of peripheral bypass grafts. *Journal of Biomechanical Engineering* 2005; **127**(7):1087–1098.
25. Giordana S. Geometrical reconstruction from medical images, classification and modelling of arterial bypass grafts. *Ph.D. Thesis, Aeronautical Engineering, Imperial College London, UK* 2004.
26. Perona P, Malik J. Scale-space and edge detection using anisotropic diffusion. *IEEE Transactions on Pattern Analysis and Machine Intelligence* 1990; **12**(7):629–639.
27. Weickert J, Benhamouda B. Why Perona-Malik filter works. *Technical Report DIKU-TR97/22, Department of Computer Science, University of Copenhagen, Denmark* 1997.
28. Otsu N. A threshold selection method from grey-level histograms. *IEEE Transactions on Systems, Man, and Cybernetics* 1979; **SMC-9**(1):62–66.
29. Kittler J, Illingworth J. Minimum error thresholding. *Pattern Recognition* 1986; **19**(1):41–47.
30. Bloomenthal J. An implicit surface polygonizer. *Graphics gems IV* 2004; pp. 324–349, Academic Press Professional Inc., San Diego, CA, USA.
31. Tobor I, Reuter P, Schlick C. Efficient Reconstruction of Large Scattered Geometric Datasets using the Partition of Unity and Radial Basis Functions. *Research Report RR-1301-03, Laboratoire Bordelais de Recherche en Informatique, Université Bordeaux* 2003.
32. Pouderoux J, Gonzato J, Tobor I, Guitton P. Adaptive hierarchical RBF interpolation for creating smooth digital elevation models. *Proc. Geographic information systems, Washington DC, USA, November* 2004; pp. 232–240.
33. Kobbelt L, Campagna S, Vorsatz J, Seidel PH. Interactive multi-resolution modeling on arbitrary meshes. *Proc. International Conference on Computer Graphics and Interactive Techniques, Orlando, USA* 1998; pp. 105–114.
34. Desbrun M, Meyer M, Schröder P, Barr AH. Implicit Fairing of Irregular Meshes using Diffusion and Curvature Flow. *Proc. International Conference on Computer Graphics and Interactive Techniques* 1999; pp. 317–324.
35. Taubin G. Curve and surface smoothing without shrinkage. *Proc. Fifth International Conference on Computer Vision,* June 1995, Massachusetts, USA; pp.852–857.
36. Cho YI, Kensey KR. Effects of the non-Newtonian viscosity of blood flows in a diseased arterial vessel. Part I: steady flows. *Biorheology* 1991; **28**(3-4):241–262.
37. Kim S, Cho YI, Jeon AH, Hogenauer B, Kensey KR. A new method for blood viscosity measurements. *Journal of non-Newtonian Fluid Mechanics* 2000; **94**(1):47–56.
38. Weinberg PD, Ethier CR. Twenty-fold difference in hemodynamic wall shear stress between murine and human aortas. *Journal of Biomechanics* 2007; **40**(7):1594–1598.
39. Shadden SC, Taylor CA. Characterization of coherent structures in the cardiovascular system. *Annals of Biomedical Engineering* 2008; **36**(7):1152–1162.
40. Jeong J, Hussain F. On the identification of a vortex. *Journal of Fluid Mechanics* 1995; **285**:69–94.
41. Hunt JCR, Wray AA, Moin P. Eddies, streams, and convergence zones in turbulent flows. *Studying Turbulence Using Numerical Simulation Databases, 2. Proceedings of the 1988 Summer Program* 1988; pp. 193–208.
42. Perry AE, Chong MS. A description of eddying motions and flow patterns using critical-point concepts. *Ann. Rev. Fluid Mech.* 1987; **19**:125–155.
43. Chakraborty P, Balachandar S, Adrian RJ. On the relationships between local vortex identification schemes. *Journal of Fluid Mechanics* 2005; **535**:189–214.
44. Levy Y, Degani D, Seginer A. Graphical visualization of vortical flows by means of helicity. *American Institute of Aeronautics and Astronautics* 1990; **28**(8):1347–1352.

45. Chong MS, Perry AE, Cantwell BJ. A general classification of three-dimensional flow fields. *Physics of Fluids A* 1990; **2**(5):765–777.
46. da Silva CB, Pereira JCF. Invariants of the velocity-gradient, rate-of-strain, and rate-of-rotation tensors across the turbulent/nonturbulent interface in jets. *Physics of Fluids* 2008; **20**(5), 055101.
47. Longest PW, Vinchurkar S. Effects of mesh style and grid convergence on particle deposition in bifurcating airway models with comparisons to experimental data. *Medical Engineering and Physics* 2007, **29**(3):350–366.
48. Butler JP, Tsuda A. Effect of convective stretching and folding on aerosol mixing deep in the lung, assessed by approximate entropy. *Journal of Applied Physiology* 1997; **83**(3):800–809.
49. Jones SW. The enhancement of mixing by chaotic advection. *Physics of Fluids A* 1991; **3**(5):1081–1086.
50. Ottino JM. The kinematics of mixing: stretching, chaos and transport. *Cambridge University Press* 1989.
51. Fountain GO, Khakhar DV, Mezic I, Ottino JM. Chaotic mixing in a bounded three-dimensional flow. *Journal of Fluid Mechanics* 2000; **417**:265–301.
52. Wang W, Manas-Zloczower I. Entropic Characterization of Distributive Mixing in Polymer Processing Equipment. *American Institute of Chemical Engineers Journal* 2003; **49**(7):1637–1644.
53. Kang TG, Kwon TH. Colored Particle Tracking Methods for Mixing Analysis of Caotic Micromixers. *Journal of Micromechanics and Microengineering* 2004; **14**(7):891–899.
54. Alemaskin K, Camesasca M, Manas-Zloczower I, Kaufman M. Entropic Measures of Mixing Tailored for Various Applications. *Proc. 8th International Conference on Numerical Methods in Industrial Forming Processes* 2004; **712**(1):169–173.
55. Gambaruto AM. Form and Flow in Anatomical Conduits: Bypass Graft and Nasal Cavity. *Ph.D Thesis, Aeronautical Engineering, Imperial College London, UK* 2007.
56. Lee KL. Coronary Flow: Magnetic Resonance Measurement and Computational Prediction. *PhD thesis, Dept. of Aeronautics, Imperial College London* 2006.
57. Khakhar DV, Rising H, Ottino JM. Analysis of chaotic mixing in two model systems. *Journal of Fluid Mechanics* 1986; **172**:419–451.
58. Kim HJ, Beskok A. Quantification of chaotic strength and mixing in a micro fluidic system. *Journal of Micromechanics and Mircroengineering* 2007; **17**(2):2197–2210.
59. Krasnopolskaya TS, Meleshko VV, Peters GWM, Meijer HEH. Mixing in Stokes flow in an annular wedge cavity. *European Journal of Mechanics - B/Fluids* 1999; **18**(5):793–822.
60. Lagana K, Balossino R, Migliavacca F, Pennati G, Bove EL, de Leval MR, Dubini G. Multiscale modeling of the cardiovascular system: application to the study of pulmonary and coronary perfusions in the univentricular circulation. *Journal of Biomechanics* 2005; **38**(5):1129–1141.
61. Formaggia L, Quarteroni A, Veneziani A. The circulatory system: from case studies to mathematical modelling. *In: Complex Systems in Biomedicine. Quarteroni and A. and Formaggia L. and Veneziani A. eds.* 2006: pp. 243–287.